Key Points:

- This study presents a new physics option for Noah-MP that accounts for canopy-induced turbulence in the roughness sublayer
- Simulated SWE over shrublands using the new turbulence scheme agree more with observations than those using the traditional MOST scheme
- Differences in snow simulations are mainly attributable to differences in aerodynamic resistance to sensible heat below the canopy top

Correspondence to:

R. Abolafia-Rosenzweig,
abolafia@ucar.edu

Implementation and Evaluation of a Unified Turbulence Parameterization Throughout the Canopy and Roughness Sublayer in Noah-MP Snow Simulations

Ronnie Abolafia-Rosenzweig[1] [ID], **Cenlin He[1]** [ID], **Sean P. Burns[1,2]** [ID], and **Fei Chen[1]** [ID]

[1]National Center for Atmospheric Research, Boulder, CO, USA, [2]Department of Geography, University of Colorado, Boulder, CO, USA

Abstract The Noah-MP land surface model (LSM) relies on the Monin-Obukhov (M-O) Similarity Theory (MOST) to calculate land-atmosphere exchanges of water, energy, and momentum fluxes. However, MOST flux-profile relationships neglect canopy-induced turbulence in the roughness sublayer (RSL) and parameterize within-canopy turbulence in an ad hoc manner. We implement a new physics scheme (M-O-RSL) into Noah-MP that explicitly parameterizes turbulence in RSL. We compare Noah-MP simulations employing the M-O-RSL scheme (M-O-RSL simulations) and the default M-O scheme (M-O simulations) against observations obtained from 647 Snow Telemetry (SNOTEL) stations and two AmeriFlux stations in the western United States. M-O-RSL simulations of snow water equivalent (SWE) outperform M-O simulations over 64% and 69% of SNOTEL sites in terms of root-mean-square-error (RMSE) and correlation, respectively. The largest improvements in skill for M-O-RSL occur over closed shrubland sites, and the largest degradations in skill occur over deciduous broadleaf forest sites. Differences between M-O and M-O-RSL simulated snowpack are primarily attributable to differences in aerodynamic conductance for heat underneath the canopy top, which modulates sensible heat flux. Differences between M-O and M-O-RSL within-canopy and below-canopy sensible heat fluxes affect the amount of heat transported into snowpack and hence change snowmelt when temperatures are close to or above the melting point. The surface energy budget analysis over two AmeriFlux stations shows that differences between M-O and M-O-RSL simulations can be smaller than other model biases (e.g., surface albedo). We intend for the M-O-RSL physics scheme to improve performance and uncertainty estimates in weather and hydrological applications that rely on Noah-MP.

Plain Language Summary Most widely used computer models of the land surface neglect canopy-induced turbulence in calculations of heat, water, and momentum exchanges. Accounting for canopy-induced turbulence is important because coherent eddies that form near the canopy top are responsible for generating most of the transportation of heat, water, and momentum, in and directly above the canopy. In 2007, 2008 scientists Ian N. Harman and John J. Finnigan developed a methodology that adapts contemporarily used equations in operational LSMs to account for canopy-induced turbulence. In this study, we create a new physics option for the Noah with Multi-Parameterization (Noah-MP) LSM that accounts for canopy-induced turbulence based on the Harman and Finnigan, 2007–2008 methodology. The primary focus of this study is to quantify differences between Noah-MP snowpack simulations using the classical physics option that neglects canopy-induced turbulence with the new physics option that accounts for canopy-induced turbulence. Overall, simulations using the new physics option tend to have better agreement with ground-based SWE observations across 647 validation sites within the western United States. We intend for the new physics scheme to improve weather and hydrological applications for operational modeling systems that rely on the Noah-MP LSM.

1. Introduction

Land surface models (LSMs) simulate terrestrial water and surface energy budgets as a key component of drought and flood predictions (Peters-Lidard et al., 2021; Sheffield et al., 2012; Viterbo et al., 2020), climate projections (Chotamonsak et al., 2011; Kurkute et al., 2020), weather predictions (Xia et al., 2015), and climate data records (Livneh et al., 2013; Maurer et al., 2002; Xia, Ek, et al., 2012; Xia, Mitchell, et al., 2012; Y. Zhang et al., 2018). Predicting terrestrial water and surface energy budgets requires accurate representation

Investigation: Ronnie Abolafia-Rosenzweig, Cenlin He, Fei Chen
Methodology: Ronnie Abolafia-Rosenzweig, Cenlin He, Fei Chen
Project Administration: Fei Chen
Supervision: Cenlin He, Fei Chen
Validation: Ronnie Abolafia-Rosenzweig, Cenlin He, Sean P. Burns
Visualization: Ronnie Abolafia-Rosenzweig
Writing – original draft: Ronnie Abolafia-Rosenzweig
Writing – review & editing: Ronnie Abolafia-Rosenzweig, Cenlin He, Sean P. Burns, Fei Chen

of water, energy and momentum exchanges between the land surface and the atmosphere (Goudriaan, 1977; Harman, 2012; Raupach et al., 1996; Raupach & Thom, 1981; Yi, 2008). LSMs often rely on a form of the Monin-Obukhov similarity theory (MOST) to calculate these exchanges (Bonan, 1996; Bonan et al., 2018; Niu et al., 2011; Niu & Yang, 2004). However, the MOST flux-profile relationships are known to fail within and above rough surfaces because these relationships make incorrect assumptions concerning the structure of turbulence in the roughness sublayer (RSL; Finnigan et al., 2009; Harman, 2012). This study is motivated by the idea that uncertainty in LSM simulations over vegetated areas is at least partially attributable to the neglect of RSL turbulence physics. In this study, we integrate a RSL turbulence parameterization with the Noah with Multi-Parameterization (Noah-MP, Niu et al., 2011) LSM and evaluate its impact on simulated seasonal evolution of snowpack over the western contiguous United States (CONUS).

Standard forms of the MOST provide a consistent set of flux-profile relationships for the atmospheric surface layer above smooth surfaces and well above rough surfaces (Högström, 1996; Monin & Obukhov, 1954). However, it has long been known that these relationships fail within canopies and in the RSL that extends to twice the canopy height or more (Bonan et al., 2018; Fazu & Schwerdtfeger, 1989; Garratt, 1978, 1994; Harman & Finnigan, 2007, 2008; Thom et al., 1975) (Figure 1). Specifically, the MOST does not consider large coherent eddies that form near the canopy top that are responsible for generating most of the turbulent kinetic energy and transport in the RSL (Finnigan et al., 2009). These turbulent structures are responsible for the majority of turbulent exchange of momentum and turbulent kinetic energy in the canopy/RSL (Finnigan et al., 2009; Finnigan & Shaw, 2000; Harman, 2012). This critical remark is not meant to detract from the value of results obtained using MOST calculations; however, the discrepancies between MOST-predicted profiles and observations within and above rough surfaces indicate the necessity of developing the theory further to establish a more generalized system of predicting flux-profiles. Consequentially, in the past 15 years, studies have focused on modifying the MOST to a more generalized form that accounts for canopy-induced turbulence in the RSL (Bonan et al., 2018; Harman, 2012; Harman & Finnigan, 2007, 2008; Novick & Katul, 2020).

Harman and Finnigan (2007, 2008) derived a formulation that modified the traditional MOST to account for the RSL turbulence; hereon termed HF08. Their theoretical formulation solves turbulent fluxes above and within the vegetation, coupling the system of equations at the canopy top to force continuity. This theory has been validated over a variety of vegetation types and densities against observed profiles of wind speed, friction velocity, surface energy budget radiation and turbulent fluxes, and turbulent exchange coefficients for momentum, moisture, and heat (Bonan et al., 2018; Harman & Finnigan, 2007, 2008; Shapkalijevski et al., 2016). These efforts showed that HF08 typically outperforms standard MOST predictions; however, HF08 has difficulty modeling scalar profiles in highly stable conditions and within the canopy (Bonan et al., 2018; Harman & Finnigan, 2007, 2008). Harman (2012) compared the standard MOST with HF08 within a simple model in a proof-of-concept study that emphasized that HF08 calculates flux-profiles within and above rough surfaces that are substantially different from MOST calculations, thus highlighting the importance of parameterizing canopy-induced turbulence in physical models. Bonan et al. (2018) was the first to apply the HF08 formulation within a sophisticated LSM, the Community Land Model-multilayer canopy model (CLM-ml v0; https://github.com/gbonan/CLM-ml_v0). Bonan et al. (2018) supports Harman's (2012) argument to parameterize canopy-induced turbulence within LSM flux-profile formulations, by finding that CLM-ml v0 had better agreement with observed energy, water and momentum flux-profiles over 12 AmeriFlux sites, relative to CLM4.5 simulations that applied the standard MOST.

These recent efforts to parameterize the RSL turbulence were motivated to improve the representation of lower atmospheric boundary conditions (Bonan et al., 2018; Harman, 2012). However, parameterizing the RSL turbulence is also expected to alter simulations of the terrestrial water budget. For example, Harman (2012) and Bonan et al. (2018) each reported that latent and sensible heat flux are sensitive to canopy-induced turbulence in the RSL. Therefore, we hypothesize that parameterizing the RSL turbulence will alter representations of terrestrial hydrologic processes that are sensitive to these turbulent heat fluxes. For example, previous work concluded that simulated snow water equivalent (SWE) is sensitive to different forms of the MOST—that is, integrating the MOST between a reference height (upper boundary) within the surface layer and the roughness length (lower boundary) versus the more general MOST (Brutsaert, 1982; Chen et al., 1997, 2014; Jiang et al., 2020; You et al., 2020; Zhang et al., 2016). However, effects of the RSL
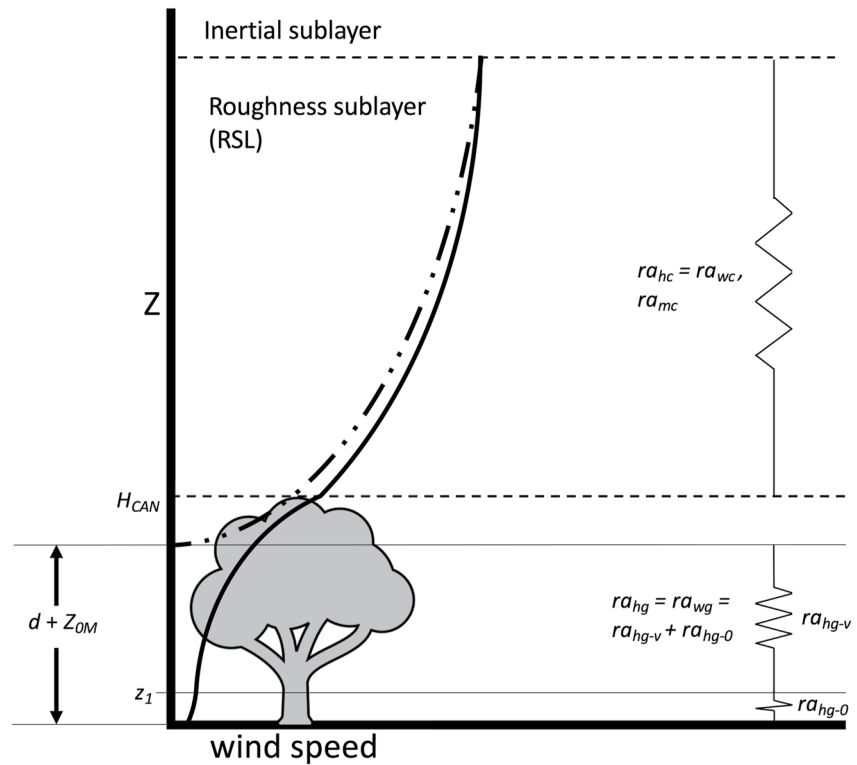
Figure 1. Conceptual example of the extrapolated Monin-Obukhov similarity theory (MOST) wind profile (dashed line) and an "observed" wind profile (solid line). The extrapolated MOST profile becomes zero at the zero-plane displacement (d) plus roughness length for momentum (Z_{0m}) height. Note the deviation between the MOST profile and the observed profile in the RSL. The observed profile is characterized as a logarithmic profile in the RSL, an exponential profile within the canopy and again a logarithmic profile below the canopy ($<z_1$) (Harman & Finnigan, 2007; Mahat et al., 2013). Within-canopy and below-canopy aerodynamic resistances for heat and water vapor (ra_{hg} and ra_{wg}) and above-canopy aerodynamic resistances for heat, water vapor, and momentum (ra_{hc}, ra_{wc}, and ra_{mc}) regulate the turbulent fluxes below and above the canopy top, respectively. The canopy top is denoted by H_{CAN}.

turbulence representation on snowpack evolution and related hydrological processes have not been systematically investigated.

The importance of snow in climate systems cannot be overstated. Snow cover fundamentally changes land-surface water and energy budgets due to high albedo, low thermal conductivity, and its control on energy and water exchange with the soil and atmosphere (Chen et al., 2014; Cohen, 1994; Dong, 2018; Ikeda et al., 2021; Rasmussen et al., 2011). Additionally, over one-sixth of the world's population rely on snowmelt as a fresh water supply (Dong, 2018; Huning & AghaKouchak, 2020). Due to the importance of predicting snowpack, the National Weather Service has a critical interest in improving snow modeling in the western CONUS (Franz et al., 2008; Mote, 2003). Previous studies have attributed errors in simulated snow states partially to the limitations of standard MOST applications in LSMs (Chen et al., 2014; You et al., 2020; Zhang et al., 2016). Given the wide use of the Noah-MP LSM within both research and operational systems, such as the Weather Research and Forecasting (WRF) model and the National Water Model (Gochis et al., 2015), it is critical to understand how Noah-MP predicted snowpack will respond to parameterizing the RSL turbulence. Therefore, the overarching goal of this study is to address the following questions: (1) *are snowpack simulations from Noah-MP sensitive to the parameterization of the RSL turbulence?* and (2) *does parameterizing the RSL turbulence improve agreement between snowpack simulations and observations?*

Our study evaluates Noah-MP simulated snowpack through implementing a new parameterization scheme of canopy-induced turbulence in the RSL based on HF08. This study is unique from previous studies that were motivated to explore RSL effects on the lower boundary layer of atmospheric models (Bonan et al., 2018; Finnigan et al., 2009; Harman, 2012). Additionally, this study is unique in scale, using 649

validation sites. The new scheme is evaluated during the 2009–2018 water years (WYs) using observations from 647 snowpack telemetry (SNOTEL) sites and two AmeriFlux sites. This study's description on the implementation of the new turbulence scheme and the corresponding evaluations provides necessary insights on future model development and improvement. The model code is publicly available (https://github.com/RAbolafiaRosenzweig/NoahMP_CanopyTurbulence) and will be included in the future Noah-MP model release.

2. Materials and Methodology

2.1. Noah-MP Land Surface Model Simulations

Noah-MP, developed based on Noah-v3.0 (Chen et al., 1996, 1997; Chen & Dudhia, 2001; Ek et al., 2003), contains multiple physics options to calculate water and energy processes (Niu et al., 2011; Yang et al., 2011). Noah-MP considers a three-layer snowpack depending on snow depth, which allows it to simulate snow variables more accurately than Noah. Further details of Noah-MP snowpack treatment can be found in Niu et al. (2011) and Chen et al. (2014). Multiple physics options within Noah-MP provide the unique ability to run a multi-model ensemble using a single LSM (Hong et al., 2014; Li et al., 2019, 2020; Yang et al., 2011; You et al., 2020; Zhang et al., 2016). In experiments conducted herein, model-physics options are selected to match the WRF/Noah-MP options used in the continental-scale convection-permitting regional climate simulations (He et al., 2019; Liu et al., 2017). Noah-MP snow-related parameters follow the values used in the latest release of WRF version 4.3 (https://github.com/wrf-model/WRF/tree/release-v4.3), where the snow cover parameter has been updated, using the default physics options, to improve simulated surface albedo and temperature. Leaf and stem area indices (LAI and SAI) are classified by vegetation type based on the Moderate Resolution Imaging Spectroradiometer (MODIS) monthly climatology from 2000 to 2008 (Yang et al., 2011). Quantitative results presented in this manuscript may change depending on different model-physics options and parameters; however, comprehensively assessing model sensitivity to various combinations of physics options available within Noah-MP such as in Zhang et al. (2016), Li et al. (2019) and Zhang et al. (2020) is beyond the scope of this study.

The focus of this study is to analyze a new physics option in Noah-MP for surface exchange coefficient for heat (SFC) and aerodynamic resistance (RAGRB) calculations in comparison to the existing physics option used in continental-scale convection-permitting regional climate simulations (He et al., 2019; Liu et al., 2017). The existing physics option, used for benchmarking, is based on the general MOST (Brutsaert, 1982), hereinafter, M-O. The new Noah-MP physics option that we introduce is based on HF08, hereon-after, M-O-RSL. M-O-RSL is an adaptation of the canopy turbulence scheme integrated into CLM-ml (Bonan et al., 2018; https://github.com/gbonan/CLM-ml_v0). A fundamental difference in the structure of Noah-MP relative to CLM-ml is that Noah-MP uses a one-layer bulk canopy model whereas CLM-ml models a multilayer plant canopy accounting for heterogeneity in the vertical structure of the foliage (Bonan et al., 2018, 2021). This governs differences in implementation and results between this study and Bonan et al. (2018, 2021).

Section 2.2 details M-O-RSL mathematically and highlights key differences between M-O-RSL and M-O. Experiments conducted in this study compare Noah-MP offline simulations using the default M-O scheme, hereinafter M-O simulations, with those using the new M-O-RSL scheme that accounts for canopy-induced turbulence in the RSL, hereinafter M-O-RSL simulations. In all simulations, land surface states are initialized using a 10-year spin-up (October 1, 2008 to September 30, 2009; 10 times in series). M-O and M-O-RSL simulations are then run for 10-years (October 1, 2008 to September 30, 2018) driven by hourly atmospheric forcing over 647 SNOTEL locations and two AmeriFlux locations: Niwot Ridge (NR) and The Glacier Lakes Ecosystem Experiments Site (GLEES) (Figure 2). For simulations at SNOTEL sites, precipitation and surface temperature forcings are scaled to match daily SNOTEL observations. All the other forcing variables—humidity, wind velocity, pressure, downward solar, and longwave radiation—are downscaled from hourly 0.125° North American Land Data Assimilation system version 2 (NLDAS-2) (Xia et al., 2009; Xia, Mitchell, et al., 2012) data to 90-m resolution with topographic adjustment following Liston and Elder (2006) and Sen Gupta and Tarboton (2016). The model vegetation cover and elevation are based on 30-m data from the National Land Cover Database (NLCD) (Wickham et al., 2021) and the Shuttle Radar Topography Mission (DOI:/10.5066/F7K072R7), respectively. Simulations at the two AmeriFlux sites use in situ observed mete-
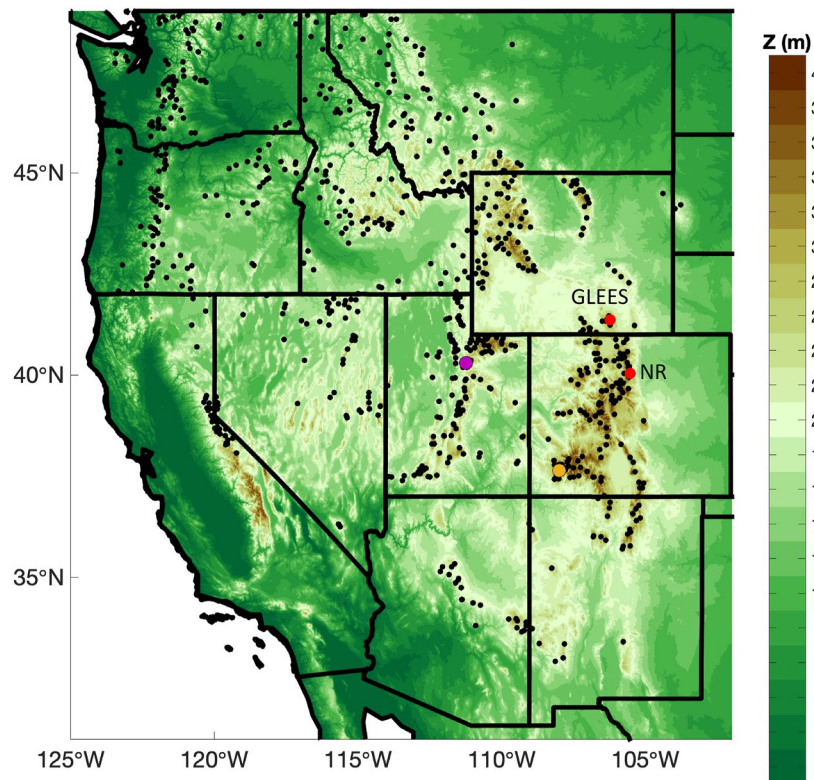
Figure 2. SNOTEL (black dots) and AMERIFLUX (red dots) site locations overlain on elevation map. Purple- and yellow-colored dots show locations of the representative closed shrubland site in Utah and deciduous broadleaf forest site in Colorado, respectively (Section 4.1.1).

orology for all forcing fields. In the case of GLEES, observed precipitation at this site is unrealistically large, so precipitation observed at the nearest SNOTEL location (~900 m away) is used in simulations instead. For NR, observed precipitation at both this site and the nearest SNOTEL site (~350 m away) is lower than accumulated SWE during multiple water years. The exact cause of these observational errors is unknown. It may be reasonable to attribute it to snow drifting, snow density uncertainty, or undercatch (Chen et al., 2014; Serreze et al., 2001). Therefore, the NR AmeriFlux precipitation is adjusted in cases where daily SWE accumulation exceeds observed precipitation accumulation, and total precipitation is back-calculated assuming the SWE increase is equal to snowfall with rain-snowfall partitioning fractions derived from the widely used Jordan (1991) parameterization.

2.2. Parameterizing the Roughness Sublayer: Comparing M-O-RSL With M-O

Here, we compare key components of the M-O-RSL scheme with the M-O scheme. We refer readers to Bonan et al. (2018) for a comprehensive and general presentation of the M-O-RSL scheme. We follow the coordinate system presented in Bonan et al. (2018) where z is the physical height above the ground rather than the Harman and Finnigan (2007, 2008) presentation where the origin is set at the top of the canopy. The M-O-RSL scheme assumes a dense and horizontally homogenous canopy, where dense means that most of the momentum is absorbed by plant elements. Harman and Finnigan (2007, 2008) found that the HF08 methodology in which M-O-RSL is based tends to be less accurate in the lower canopy where the vegetation density is more complex. This is important in the context of snow modeling, where within-canopy and below-canopy turbulent heat flux often modulates snowpack evolution (Burns et al., 2014; Mahat et al., 2013). Notwithstanding, the M-O-RSL formulation is considered a computationally efficient and valuable update to M-O that can be implemented within sophisticated LSMs (Bonan et al., 2021). Although the M-O scheme is based on the MOST, there are discrepancies between the M-O formulation and the standard MOST in which M-O-RSL was adapted from (Bonan et al. [2018] and Harman and Finnigan [2007, 2008]).

Hence, discrepancies between M-O and M-O-RSL are not solely attributable to parameterizing the RSL in M-O-RSL (see Sections 2.2.1 and 2.2.2 for details). Table S1 presents the symbols used in Equations 1–24 that describe M-O and M-O-RSL formulations.

2.2.1. Wind Speed at Canopy Top

Neglecting the RSL, M-O describes wind speed at the canopy top (U_C) based on the logarithmic decay of the wind profile above the canopy predicted from MOST (Figure 1):

$$U_C = \frac{u_*}{k} \times \ln\left(\frac{H_{CAN} - d}{Z_{0M}}\right) \tag{1}$$

where u_* is the friction velocity, k is the von Kármán constant ($k = 0.4$), H_{CAN} is canopy height, Z_{0M} is the vegetation roughness length for momentum, and d is zero-plane displacement. In M-O, d is calculated using Equation 2,

$$d = 0.65 H_{CAN} \tag{2}$$

whereas M-O-RSL computes d using Equation 3,

$$d = H_{CAN} - \beta^2 L_c \left(1 - e^{-\frac{0.25 VAI}{\beta^2}}\right) \tag{3}$$

M-O-RSL solves for U_C based on the Harman and Finnigan (2007, 2008) formulation:

$$U_C = \frac{u_*}{\beta} \tag{4}$$

In M-O, u_* is solved as:

$$u_* = \frac{U_R k}{\left[\ln\left(\dfrac{Z_{ref} - d}{Z_{0M}}\right) - \varphi_m\left(\dfrac{Z_{ref} - d}{L_{MO}}\right)\right]} \tag{5}$$

and in M-O-RSL, u_* is solved as:

$$u_* = \frac{U_R k}{\left[\ln\left(\dfrac{Z_{ref} - d}{H_{CAN} - d}\right) - \varphi_m\left(\dfrac{Z_{ref} - d}{L_{MO}}\right) + \varphi_m\left(\dfrac{H_{CAN} - d}{L_{MO}}\right) + \hat{\varphi}_m\left(Z_{ref}\right) - \hat{\varphi}_m\left(H_{CAN}\right) + \dfrac{k}{\beta}\right]} \tag{6}$$

where U_R is the observed wind speed at the reference height (Z_{ref}), φ_m adjusts the log profile in relation to the Obukhov length (L_{MO}), and $\hat{\varphi}_m$ adjusts the profile to account for canopy-induced turbulence in the RSL. β is calculated based on Equations 7 and 8. For stable conditions, when L_{MO} exceeds 0, β is derived as:

$$\beta = -\left[0.5\left(\sqrt{\left(-27\beta_N\left(\frac{5L_C}{L_{MO}}\right)^2\right)^2 + 4\left(15\frac{L_c}{L_{MO}}\right)^3} - 27\beta_N\left(\frac{5L_c}{L_{MO}}\right)^2\right)\right]^{\frac{1}{3}} \times \frac{L_{MO}}{15L_c}$$

$$+ \left[0.5\left(\sqrt{\left(-27\beta_N\left(\frac{5L_C}{L_{MO}}\right)^2\right)^2 + 4\left(15\frac{L_c}{L_{MO}}\right)^3} - 27\beta_N\left(\frac{5L_c}{L_{MO}}\right)^2\right)\right]^{-\frac{1}{3}} \tag{7}$$

For unstable conditions ($L_{MO} < 0$), β is derived as:

$$\beta = \sqrt{0.5\left[-\left(\frac{16\beta_N^4 L_c}{L_{MO}}\right) + \sqrt{\left(\frac{16\beta_N^4 L_c}{L_{MO}}\right)^2 + 4\beta_N^4}\right]} \tag{8}$$

where β_N is the value for β at neutral conditions ($\beta_N = 0.35$; Bonan et al., 2018). The solution for β is constrained between 0.2 and 0.5 (Bonan et al., 2018). L_{MO} is solved for in both M-O and M-O-RSL as:

$$L_{MO} = \frac{u_*^2 \theta_{vref}}{kg\theta_{v*}} \tag{9}$$

where θ_{vref} is the virtual potential temperature at the reference height, θ_{v*} is the virtual potential temperature scale, g is the acceleration due to gravity, and L_c is the canopy length scale:

$$L_c = \frac{H_{CAN}}{c_d \times VAI} \tag{10}$$

c_d is the dimensionless leaf aerodynamic drag coefficient ($c_d = 0.25$; Bonan et al., 2018) and VAI is the sum of LAI and SAI.

2.2.2. Aerodynamic Resistances for Momentum, Heat, and Water Vapor

Noah-MP requires solving for aerodynamic resistances for momentum (ra_{mc}), sensible heat (ra_{hc}), and water vapor (ra_{wc}) above the canopy ($Z_{ref} > z \geq H_{CAN}$). We note that Noah-MP assumes ra_{wc} to be the same as ra_{hc}. M-O and M-O-RSL solve for ra_{mc} using:

$$ra_{mc} = \frac{U_R}{u_*^2} \tag{11}$$

where differences between M-O and M-O-RSL ra_{mc} solutions are based on differences in u_* (i.e., Equations 5 and 6, respectively). M-O solves for ra_{hc} following Bonan (1996):

$$ra_{hc} = \frac{1}{ku_*}\left[\ln\left(\frac{Z_{ref}-d}{Z_{0H}}\right) - \varphi_H\left(\frac{Z_{ref}-d}{L_{MO}}\right)\right] = \frac{1}{k^2 \times U_R}\left[\ln\left(\frac{Z_{ref}-d}{Z_{0M}}\right) - \varphi_m\left(\frac{Z_{ref}-d}{L_{MO}}\right)\right]$$
$$\left[\ln\left(\frac{Z_{ref}-d}{Z_{0H}}\right) - \varphi_h\left(\frac{Z_{ref}-d}{L_{MO}}\right)\right] \tag{12}$$

whereas M-O-RSL amends Equation 12 to account for the RSL using Equation 13.

$$ra_{hc} = \frac{1}{ku_*}\left[\ln\left(\frac{Z_{ref}-d}{H_{CAN}-d}\right) - \varphi_h\left(\frac{Z_{ref}-d}{L_{MO}}\right) + \varphi_h\left(\frac{H_{CAN}-d}{L_{MO}}\right) + \hat{\varphi}_h(Z_{ref}) - \hat{\varphi}_h(H_{CAN})\right] \tag{13}$$

Z_{0H} is the vegetation roughness length for sensible heat, and the stability functions for heat and momentum, φ_h and φ_m, adjusts the log profile in relation to the Obukhov length. Equation 13 also introduces the RSL function, $\hat{\varphi}_h$, which adjusts the profile to account for canopy-induced physics in the RSL. $\hat{\varphi}_h$ and $\hat{\varphi}_m$ must be integrated using numerical methods; however, in practice, the values are obtained from a lookup table provided by Bonan et al. (2018). In M-O and M-O-RSL, the surface exchange coefficient/conductance for heat from the H_{CAN} to Z_{ref} over the vegetated fraction of the pixel, C_{HV}, is equated to the inverse of ra_{hc}:

$$C_{HV} = \frac{1}{ra_{hc}} \tag{14}$$

Noah-MP solves for the aerodynamic resistance for sensible heat (ra_{hg}) within and below the canopy ($z \leq H_{CAN}$) in M-O using Equations 15 and 16 (Brutsaert, 1982; Niu & Yang, 2004):

$$ra_{hg} = \frac{H_{CAN} \times e^a}{K_c(H_{CAN}) \times a} \times \left(e^{-a\left(\frac{Z_{0HG}}{H_{CAN}}\right)} - e^{-a\left(\frac{Z_{0H}+d}{H_{CAN}}\right)} \right) \tag{15}$$

$$a = \left(\alpha \times \text{VAI} \times H_{CAN} \times \Phi_m \right)^{0.5} \tag{16}$$

where α is the canopy wind absorption parameter based on vegetation classification (Goudriaan, 1977), Φ_m is the stability correction factor for momentum, and Z_{0HG} is the ground roughness length for sensible heat. $K_c(H_{CAN})$ is the turbulent transfer coefficient for sensible heat at H_{CAN}. M-O solves for $K_c(H_{CAN})$ as:

$$K_c(H_{CAN}) = k \times u_* \times (H_{CAN} - d) \tag{17}$$

whereas M-O-RSL solves for $K_c(H_{CAN})$ as:

$$K_c(H_{CAN}) = lm \times \frac{u_*}{Sc} \tag{18}$$

where Sc is the Schmidt number and lm is the mixing length computed as:

$$lm = \frac{2\beta^3 H_{CAN}}{c_d \times \text{VAI}} \tag{19}$$

M-O-RSL solves for ra_{hg} as the summation of the resistance immediately above the ground ($ra_{hg\text{-}0}$) and the ra_{hg} profile within the canopy ($ra_{hg\text{-}v}$). $ra_{hg\text{-}0}$ is calculated as:

$$ra_{hg-0} = \frac{1}{k^2 u_1} \left[\ln\left(\frac{z_1}{Z_{0MG}}\right) \ln\left(\frac{z_1}{Z_{0HG}}\right) \right] \tag{20}$$

where Z_{0MG} is the ground roughness length for momentum, z_1 is a defined height directly above the ground, and u_1 is the wind speed at z_1. z_1 is also considered the height where flux profiles transition from exponential to logarithmic (Figure 1). z_1 is defined in this study as 5 cm to match the definition from Bonan et al. (2018). However, M-O-RSL simulations can be sensitive to the definition of z_1, as discussed in Section S1. Thus, z_1 should be considered an optimizable parameter. u_1 is derived following the HF08 methodology:

$$u_1 = U_C \times e^{\left(\frac{\beta(z_1 - H_{CAN})}{lm}\right)} \tag{21}$$

The cumulative resistance profile within the canopy is solved for as:

$$ra_{hg-v} = \frac{lm}{\beta K_c(H_{CAN})} \sum_{z_i = z_1}^{z_{i+1} = Z_{0H}+d} \left\{ e^{\left[-\frac{\beta(z_i - H_{CAN})}{lm}\right]} - e^{\left[-\frac{\beta(z_{i+1} - H_{CAN})}{lm}\right]} \right\} \tag{22}$$

where the M-O-RSL physics option discretizes the profile ranging from z_1 to $Z_{0H} + d$ into 20 homogeneous segments. Finally, ra_{hg} in M-O-RSL is computed as the summation of within-canopy and below-canopy aerodynamic resistance for sensible heat:

$$ra_{hg} = ra_{hg-v} + ra_{hg-0} \tag{23}$$

Noah-MP also assumes ra_{wg} (resistance for water vapor within and below the canopy) to be the same as ra_{hg}. In both M-O and M-O-RSL, the surface exchange coefficient/conductance for heat under the canopy top, $C_{H\text{-}UC}$, is equated to the inverse of ra_{hg}:

$$C_{H-UC} = \frac{1}{ra_{hg}} \tag{24}$$

Note, that the M-O-RSL scheme assumes the wind profile shape of the theoretical observed profile shown in Figure 1: logarithmic above the canopy top (Equation 13), exponential from the canopy top to z_1 (Equation 22), and logarithmic below z_1 (Equation 20). $ra_{hg\text{-}v}$ does not include information from $Z_{0H} + d$ to H_{CAN} to remain consistent with the profile coverage represented in the existing M-O physics option.

2.3. Snow Evaluation

We evaluate Noah-MP simulations against SWE observations over 647 SNOTEL sites that have at least one complete year of observations (Section 3.1 and Figure 2), which are commonly used to validate LSM snow simulations (Barlage et al., 2010; Chen et al., 2014; He et al., 2019; Livneh et al., 2010; Pan et al., 2003). We run all Noah-MP simulations at a 90-m spatial resolution, limited by meteorological forcing downscaling (Section 2.1), to minimize differences between simulated and observed SWE based on representativeness of the point-based observation for the bounding model grid cell. Although SNOTEL gauges are typically located in small forest clearings, Pan et al. (2003) determined that SNOTEL observed SWE is spatially correlated up to 0.25° lag distance. Thus, point-based SNOTEL measurements contain sufficient information about the surrounding area to be considered representative of the 90-m grid mean. Notwithstanding, differences between simulated and observed SWE may be partially attributable to the spatial representativeness of point-based observations, but these differences are likely small relative to differences induced by uncertainty in model physics evaluated herein, considering the very high spatial resolution of our simulations based on the accurate NLCD vegetation cover map.

In our evaluation, we first quantify the performance of M-O and M-O-RSL simulations using the mean and spatial variability of snow states across all validation SNOTEL sites. Next, we quantify the accuracy of simulated SWE on a site-by-site basis using the Pearson correlation coefficient (R) and RMSE. Subsequently, we present the importance of capturing peak SWE by correlating simulated peak SWE biases with root-mean-square-error (RMSE) calculated over the 10-year simulations. Peak SWE is then compared with ablation rates to support the idea that errors during the accumulation period propagate to the ablation period.

Skill scores are assessed in the context of climate conditions to understand if differences in model performance between M-O and M-O-RSL simulations are sensitive to local precipitation or temperature. Skill scores are then assessed in the context of vegetation classification to understand which vegetation types are most sensitive to switching from M-O to the M-O-RSL physics option. Vegetation classifications with less than 10 validation sites are not considered in this analysis. In-depth analyses are performed over vegetation types that experience the largest degradation (deciduous broadleaf forest) and improvement (closed shrubland) in skill scores. Specifically, we explore if changes in peak SWE between M-O and M-O-RSL simulations are attributable to changes in sublimation or snow melt while providing insights on how changes in peak SWE relate to surface exchange coefficients. We briefly test the sensitivity of M-O and M-O-RSL snow simulations to VAI climatology over deciduous broadleaf forest sites by using another VAI climatology from the Livneh et al. (2013) data set instead of MODIS (Section 2.1) to assess if different, but widely used, vegetation parameters substantially alter performance (Livneh et al., 2013; Maurer et al., 2002; https://ciresgroups.colorado.edu/livneh/data).

Next, we isolate differences in ablation between M-O and M-O-RSL simulations following methodology presented in Xiao et al. (2021) over two representative sites: a deciduous broadleaf forest and closed shrubland site, respectively. Representative sites are those that record the median difference in performance (i.e., RMSE of daily SWE) between M-O and M-O-RSL simulations for respective vegetation classifications. Over these sites, we adjust simulated snow predictions to match observed peak SWE magnitude, timing, and snow depth. These simulations follow the direct-insertion data assimilation technique (Robinson & Lermusiaux, 2000) by replacing simulated SWE and snow depth with observations on the date that observations record peak SWE for each water year. These simulations allow for a clear diagnosis of differences between M-O and M-O-RSL ablation that are not biased by discrepancies during the accumulation period. We only analyze years when observed peak SWE falls between the time that 80% of peak SWE is reached in the accumulation period to the time that 80% of peak SWE is reached in the ablation period from respective open loop simulations because it would be inappropriate to force peak SWE conditions in the midst of simulated

rising or falling limbs. This screening removes five out of 10 analysis years for both the representative deciduous broadleaf forest and closed shrubland site.

In analyses where accumulation or ablation periods are considered, we use the methodology from Xiao et al. (2021) to define season bounds. Specifically, accumulation periods span dates corresponding to 20% and 80% of peak SWE during the rising limb of the annual SWE cycle. Similarly, ablation periods span dates corresponding to 20% and 80% of peak SWE during the falling limb of the annual SWE cycle. Focusing on the central portion of accumulation and ablation periods provides a representation of processes that minimizes unusual conditions near the bounds of respective seasons.

2.4. AmeriFlux Surface Energy Budget and Snow Evaluation

Following Chen et al.'s (2014) methodology, we examine the relationship of the surface energy budget to SWE evolution over two AmeriFlux sites: NR in Colorado and GLEES in Wyoming. NR and GLEES are both characterized as evergreen needleleaf forests that experience severe winters and cool summers with no dry season. NR is densely vegetated, whereas GLEES has openings between large trees (Blanken et al., 2020; Massman, 2021; Frank et al., 2014; https://ameriflux.lbl.gov/sites/siteinfo/US-NR1; https://ameriflux.lbl.gov/sites/siteinfo/US-GLE). Simulations were evaluated with radiative and heat fluxes observed above the vegetation canopy, and observed SWE from nearby (<1 km) SNOTEL stations. Discrepancies between observed and simulated SWE are examined in the context of the surface energy budget:

$$S\downarrow - S\uparrow + L\downarrow - L\uparrow = Q_H + L_H + G \tag{25}$$

$S\downarrow$ and $S\uparrow$ are the downward and upward shortwave radiation, respectively. $L\downarrow$ and $L\uparrow$ are the downward and upward longwave radiation, respectively. Q_H is the sensible heat flux from the surface to the atmosphere; L_H is the latent heat flux from the surface to the atmosphere; G is the ground heat flux at the air-snowpack/soil interface. $S\downarrow$ and $L\downarrow$ are observed, and computations of other terms in Equation 25 are described in Niu et al. (2011). We note that Equation 25 does not include heat transferred to the surface by precipitation and net heat storage change in the vegetation and snow layers because these terms are relatively small compared to terms included in Equation 25 (Chen et al., 2014). The omission of these terms results in small surface energy budget closure errors, ranging from 0.01% to 0.05% of $S\downarrow$ varying by simulation.

2.5. AmeriFlux Within-Canopy Wind Speed and Turbulent Heat Flux Analysis

Within-canopy wind speed and turbulent fluxes of sensible and latent heat are important processes that govern ablation (Mahat et al., 2013). M-O and M-O-RSL have difficulties modeling these fluxes within a single-layer canopy model (i.e., Noah-MP) because of the complex canopy effects on the wind field (Bonan et al., 2021; Harman & Finnigan, 2007, 2008; Mahat et al., 2013). The Noah-MP LSM does not explicitly calculate a vertical profile for wind speed within the canopy; however, the current form of Noah-MP assumes a continuous exponential decay based on Equation 26 (e.g., Figure 1) (Brutsaert, 1982); whereas M-O-RSL assumes an exponential profile based on Equation 21.

$$u(z) = U_C e^{\left[-a\left(1 - \frac{z}{H_{CAN}}\right)\right]} \tag{26}$$

We compare simulated within-canopy wind speed based on these assumed exponential profiles from M-O and M-O-RSL with wind speed observations from GLEES at 6.5 m and NR at 5.7 m. Next, to further understand the relationship between the surface energy budget and snowpack, simulated within-canopy latent and sensible heat flux are compared with 6.5 m observations from GLEES and 5.7 m observations from NR. Burns et al. (2018) provide a critique of big-leaf type models that assume above-canopy friction velocity is linearly related with wind speed in the subcanopy by showing that these observed variables are not linearly related at Niwot Ridge. We test this assumed linear relationship further by comparing observed friction velocity at 22.5 m with wind speed observed at 5.7 m over the GLEES AmeriFlux site.
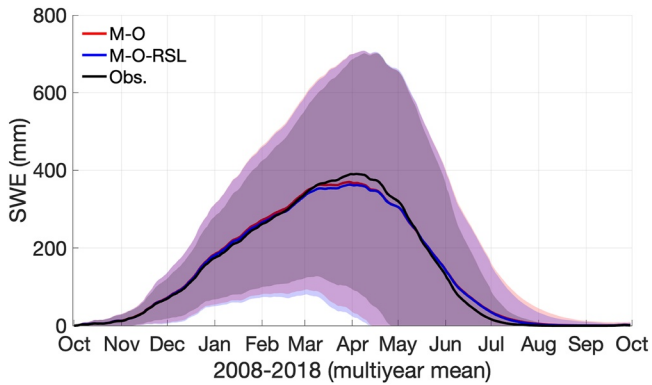
Figure 3. (a) Mean multiyear (2009–2018 WYs) time series for SWE across all SNOTEL locations (Figure 2) for M-O simulations (red), M-O-RSL simulations (blue), and SNOTEL observations (black). Shading represents one standard deviation, calculated from the spread in daily SWE across SNOTEL sites.

3. Data

3.1. SNOTEL Observations

The United States Department of Agriculture (USDA) Natural Resources Conservations Service (NRCS) SNOTEL sites were designed to provide cost-effective data from high snow accumulation regions throughout the west (Serreze et al., 1999). This analysis uses bias-corrected and quality-controlled daily SNOTEL observations from the Pacific Northwest National Laboratory (PNNL) (Sun et al., 2019; Yan et al., 2018; https://www.pnnl.gov/data-products). We evaluate differences in performance between M-O and M-O-RSL simulations relative to daily SWE observations over 647 SNOTEL sites. Daily SWE is measured using snow pillows with an antifreeze solution at each SNOTEL site. As the snow accumulates, the weight of the snowpack forces the solution into a manometer column, and the corresponding increase/decrease in manometer height is equal to the increase/decrease in SWE (Serreze et al., 1999, 2001).

3.2. AmeriFlux Observations

In the surface energy budget analysis (Sections 2.4 and 4.2), 30-min AmeriFlux observations (https://ameriflux.lbl.gov/) of upward short-wave and longwave radiation and turbulent sensible and latent heat flux are aggregated to daily time series for comparison with Noah-MP simulations. The primary focus of the analysis only considers above-canopy observations: 22.65–25.8 m for GLEES and 21.5–25.5 m for NR. This allows a fair comparison with Noah-MP outputs that are a conglomerate of vegetated and non-vegetated surfaces within model grid cells. Note that simulated G from Equation 25 is not compared with Ameriflux observations because during times when soil is covered with snow, observed soil heat flux is near zero at all times due to snow-insulation. However, simulated G from Noah-MP represents the heat flux into the snow surface for snow-covered soil. A supplementary analysis is presented that compares simulated within-canopy wind speed, sensible heat flux and latent heat flux with 6.5 m observations from GLEES and 5.7 m observations from NR (Sections 2.5 and 4.3). Within-canopy observations from NR are described in Burns et al. (2014).

4. Results and Discussions

4.1. Evaluation of SWE at SNOTEL Sites

SWE from M-O and M-O-RSL simulations strongly agree with observations averaged across all validation SNOTEL sites (R for M-O and M-O-RSL = 1.0; percent bias for M-O = 1.8%; percent bias for M-O-RSL = 0.1%; solid lines in Figure 3). M-O and M-O-RSL simulations tend to predict slower ablation than observations, but this bias is partially compensated by underestimates in peak SWE. M-O and M-O-RSL simulations agree on spatial (cross-site) variability in daily SWE across validation sites, each showing similar mean and interquartile ranges (IQRs) of daily standard deviation (mean for M-O and M-O-RSL = 147 mm; IQR for M-O = 25–254 mm; IQR for M-O-RSL = 22–256 mm). However, this is an overestimate of the observed variability with a mean standard deviation of 124 mm (IQR = 13–224 mm) (shaded areas in Figure 3). In other words, this means that observations record greater similarities in snowpack across the western CONUS than Noah-MP simulates. Figure 4 presents differences between evaluation metrics (RMSE and R) from M-O-RSL and M-O simulations across each validation site. At the majority of sites, the M-O-RSL simulation corresponds with lower RMSE (65% of sites; warmer colors in Figure 4a) and higher R (69% of sites; cooler colors in Figure 4b) than the M-O simulation. The tendency for M-O-RSL simulations to outperform M-O simulations is insensitive to site mean annual precipitation or temperature (Figure S2).

Errors calculated throughout the entirety of simulations are predominately explained by errors that occur over accumulation periods. This is supported by Figure 5a that shows biases in peak SWE strongly correlate with RMSE of daily SWE calculated throughout 10-year simulations (R for M-O simulations = 0.77; R for M-O-RSL simulations = 0.82). This relationship is stronger for M-O-RSL simulations because cases
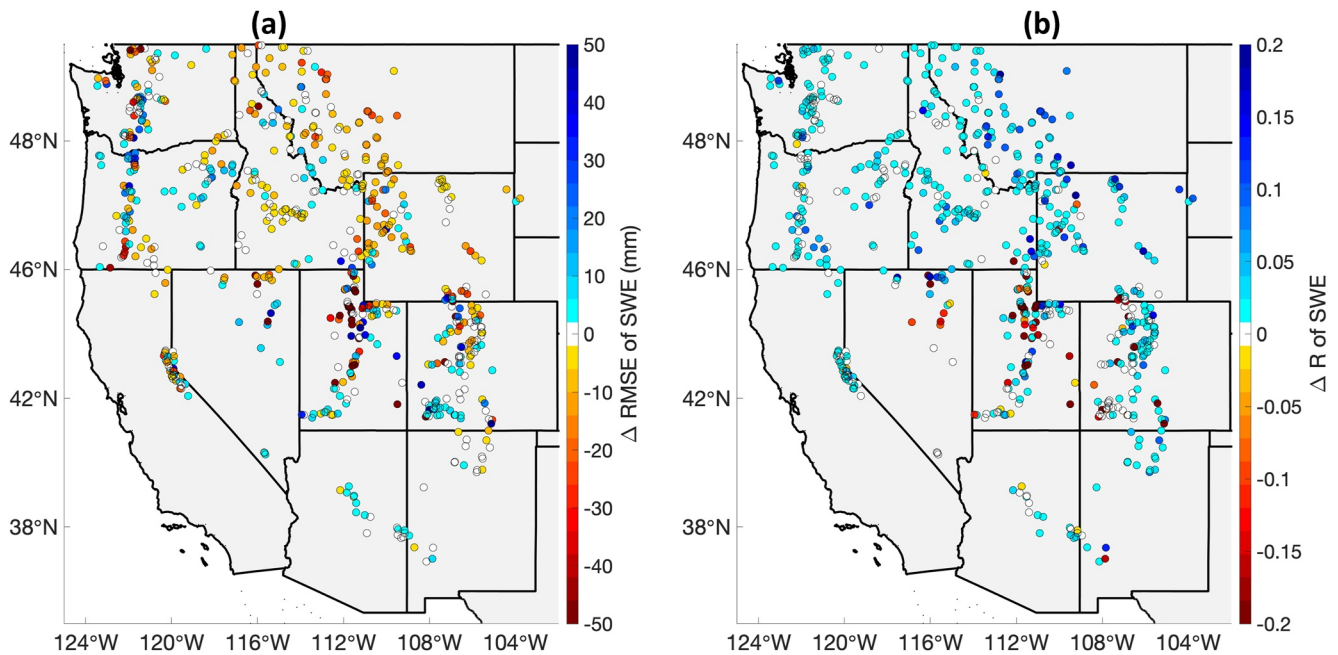
Figure 4. Difference in evaluation metrics (RMSE and R), calculated as M-O-RSL minus M-O, across each validation site. Warmer colors (yellow-red) indicate sites where M-O-RSL has a lower evaluation metric, and cooler colors (shades of blue) indicate sites where M-O-RSL has a higher evaluation metric. (a) Difference in RMSE for daily SWE over 647 SNOTEL locations. (b) Difference in R for daily SWE over 647 SNOTEL locations. Original skill scores for M-O and M-O-RSL simulations across all SNOTEL stations are reported in Table S2.

with anomalously large underestimates in peak SWE tend to be more extreme in M-O-RSL simulations. The strong correlation between peak SWE and ablation rates (Figure 5b; $R > 0.77$) further emphasizes the importance of accurately representing peak SWE. Xiao et al. (2021) suggests this strong correlation may be attributable to low SWE stations experiencing the bulk of snowmelt before the period of highest available energy. Given the importance of simulating SWE accumulation accurately, differences in peak SWE biases from M-O-RSL and M-O simulations relative to SNOTEL observations explain the majority of the difference in simulated evaluation metrics calculated throughout the entire 10-year simulation (Figure 4). Specifically, differences in peak SWE biases between M-O-RSL and M-O simulations strongly correlate with differences in overall model RMSE ($R = 0.86$) and correlation ($R = -0.67$) calculated throughout the entire 10-year duration of the study. We note that in aforementioned assessments (Figures 3–5), aggregating results across all sites mask out many details in the performance differences between M-O and M-O-RSL simulations. Additionally, this type of aggregation makes it difficult to identify mechanistic causes for differences between
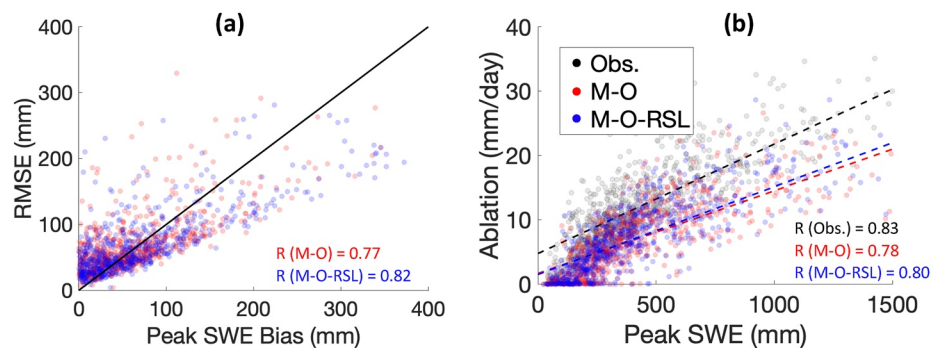

Figure 5. (a) Scatter plot comparing average biases in peak SWE (horizontal axis) with RMSE (vertical axis) for M-O and M-O-RSL simulations, relative to observed SWE, for each SNOTEL site. The solid black line represents a 1:1 reference line. (b) Scatter plot comparing average Peak SWE (horizontal axis) with ablation rates for each SNOTEL site. Respectively colored dashed lines represent best fit lines.
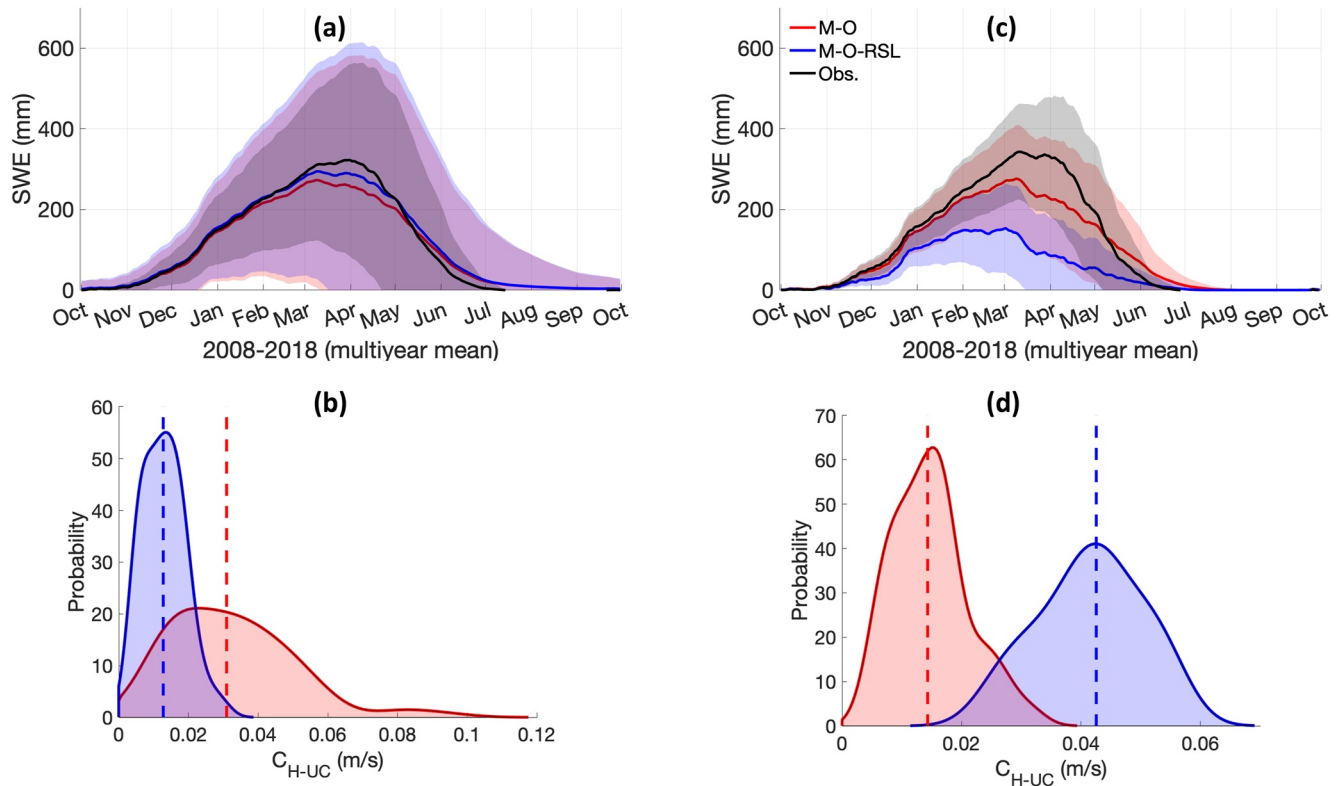
Figure 6. (a) Mean multiyear (2009–2018 WYs) time series for SWE across 84 SNOTEL sites classified as closed shrubland for M-O simulations (red), M-O-RSL simulations (blue) and SNOTEL observations (black). Shading represents one standard deviation, calculated from the spread in daily SWE across all SNOTEL sites. (b) Kernel density estimators for C_{H-UC} (Equation 24) for M-O-RSL (blue) and M-O (red) simulations over 84 closed shrubland SNOTEL sites. (c) same as (a), but for 53 deciduous broadleaf forest sites. (d) same as (b), but for 53 deciduous broadleaf forest sites.

M-O-RSL and M-O simulations. Thus, we conduct process-level analyses at selected sites in the following sections.

4.1.1. Snow Evaluation Classified by Vegetation Type

The largest improvements in M-O-RSL simulations compared with M-O simulations occur over closed shrubland (CS) sites (84 sites) where M-O-RSL has less extreme underestimates of peak SWE (Figures 6a and S3), and the largest degradation in M-O-RSL simulations compared with M-O simulations occur over deciduous broadleaf forest (DBF) sites (53 sites) where M-O-RSL has more extreme underestimates of peak SWE (Figures 6c and S3). We note that degradation in skill over DBF sites is expected because the M-O-RSL methodology assumes a dense canopy (Harman & Finnigan, 2007, 2008); an assumption violated over DBF sites in the winter. Although this assumption is also violated over CS sites, errors in the assumed exponential decay of the wind profile throughout the vegetated column play a relatively small role over CS sites where H_{CAN} is assumed to be 1.1 m, much smaller than 16 m over DBF sites. Figure 7 shows that differences in within- and below-canopy conductance for sensible heat (C_{H-UC}) between M-O and M-O-RSL simulations explains qualitative differences in peak SWE. Specifically, across all sites, 93% of the time M-O-RSL predicts higher C_{H-UC} than M-O, M-O-RSL predicts lower peak SWE (bottom right quadrant of Figure 7a). Conversely, 74% of the time M-O-RSL predicts lower C_{H-UC} than M-O, M-O-RSL predicts higher peak SWE (top left quadrant of Figure 7a). Exceptions to this trend tend to correspond with very small changes in C_{H-UC}: the mean difference for exceptions is 0.002 m/s which is 2.7 times smaller than the mean difference in C_{H-UC} averaged across all data points. Figure 7b shows that the aforementioned relationship between differences in M-O-RSL and M-O predicted C_{H-UC} and peak SWE are not robust when C_{HV} is considered instead of C_{H-UC}. Namely, 97% of the water years at each site M-O-RSL predicts higher C_{HV}, but M-O-RSL predicts lower peak SWE than M-O only 45% of the time.
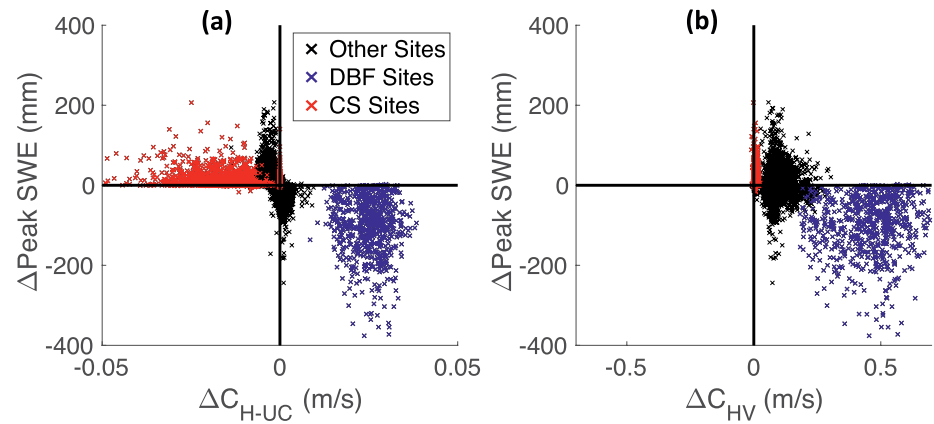
Figure 7. Differences in $C_{H\text{-}UC}$ between M-O-RSL and M-O simulations control differences in peak SWE. (a) M-O-RSL minus M-O $C_{H\text{-}UC}$ (horizontal axis) and M-O-RSL minus M-O peak SWE (vertical axis) for deciduous broadleaf forest SNOTEL sites (blue x's), closed shrubland sites (red x's) and all other sites (black x's). Differences in daily $C_{H\text{-}UC}$ are averaged from October 1 to the date of peak SWE for each water year at each of the 647 SNOTEL sites. (b) same as (a), but showing the above-canopy surface heat exchange coefficient (C_{HV}; Equation 14) on the vertical axis instead of $C_{H\text{-}UC}$.

For CS sites, M-O-RSL predicts 2.4 times lower $C_{H\text{-}UC}$ (Figure 6b) and thus higher peak SWE (i.e., better agreement with observations) 88% of the time (red x's in the top left quadrant of Figure 7a) relative to M-O. Lower $C_{H\text{-}UC}$ from M-O-RSL corresponds with less downwards sensible heat flux, and thus less heat flux into the snowpack that drives snow melt. Note that differences in peak SWE between M-O and M-O-RSL have a high correlation with differences in snowmelt during SWE accumulation ($R = -0.84$). We identify two factors that contribute toward M-O-RSL predicting higher ra_{hg} (i.e., lower $C_{H\text{-}UC}$) than M-O over CS sites. First, M-O-RSL explicitly accounts for $ra_{hg\text{-}0}$ (i.e., Equation 20) and M-O does not. Note that $ra_{hg\text{-}0}$ accounts for 64% of total ra_{hg} over closed shrubland sites. Second, M-O predicts higher U_C than M-O-RSL over closed shrubland sites, favoring larger within- and below-canopy aerodynamic conductance in M-O.

For DBF sites, M-O-RSL predicts three times higher $C_{H\text{-}UC}$ (Figure 6d) and thus lower peak SWE 99% of the time (blue x's in the bottom right quadrant of Figure 7a), relative to M-O. Higher $C_{H\text{-}UC}$ from M-O-RSL corresponds with greater downwards sensible heat flux, and thus more heat flux into the snowpack that drives snow melt. Note that differences in peak SWE between M-O and M-O-RSL have a high correlation with differences in snowmelt during SWE accumulation ($R = -0.86$). M-O-RSL predicts relatively high $C_{H\text{-}UC}$ over DBF sites partially due to calculating high wind speed directly above the ground (i.e., u_1 from Equations 20 and 21; Figure S4a). This occurs because M-O-RSL predicts relatively high U_c and weak wind speed decay throughout the vegetated profile (Figure S4a), both of which are attributable to low VAI during winter. Therefore, we test the sensitivity to VAI over DBF sites by running new M-O and M-O-RSL simulations that use Livneh et al. (2013) VAI climatology, which increases the VAI climatology at DBF sites relative to our standard simulations using the MODIS product. This change in VAI results in reduced M-O and M-O-RSL peak SWE biases by 14% and 23%, respectively (Figure S5). Bias reductions in M-O-RSL occur because higher VAI causes M-O-RSL to predict lower U_c and greater wind speed decay throughout the vegetated profile (Figure S4) which yields a $C_{H\text{-}UC}$ estimate that is three times smaller than the original. Bias reductions in M-O occur, because increased VAI increases the wind absorption parameter, a from Equations 15 and 16, which results in higher ra_{hg} (i.e., lower $C_{H\text{-}UC}$). These results indicate that simulations presented in this study can be substantially improved with optimized parameters, and are subject to change for simulations that use the dynamic vegetation physics option instead of VAI climatology.

Differences between M-O and M-O-RSL ablation are examined over a representative DBF and CS site with simulations that directly insert peak SWE and corresponding snow depth observations (Figures 2 and 8). Differences in ablation rates are qualitatively consistent from year to year (Figures 9d and 9h) so we choose to show results in Figure 8 from years that highlight the largest discrepancies between M-O-RSL and M-O simulations for illustrative purposes. Over the DBF site, the M-O-RSL simulation predicts faster ablation than the M-O simulation (Figures 8a, 8b, and 9d) because the M-O-RSL scheme calculates larger $C_{H\text{-}UC}$
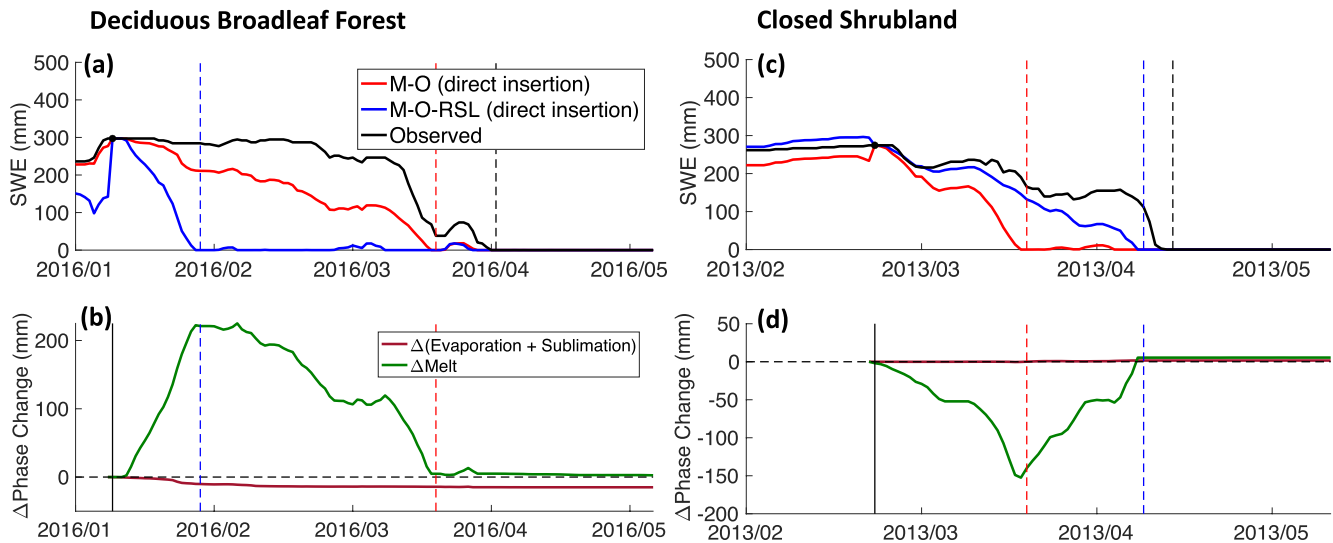
Figure 8. (a) SWE time series from simulations that directly insert observed peak SWE (black dot) from the representative deciduous broadleaf forest site. Vertical dashed lines represent the day of snow disappearance for the M-O simulation (red), the M-O-RSL simulation (blue) and observations (black). (b) Change in snow melt (green) and evaporation (maroon) for the M-O-RSL minus M-O simulation from the representative deciduous broadleaf forest site. (c, d) same as (a, b) but for the representative closed shrubland site.

(Figure 9a) causing larger downward sensible heat flux by 25 W/m² (median) and hence larger heat flux into snowpack by 26 W/m² (median) (Figure 9b), which increases both ground and snow temperatures, on average by 1.5 and 0.99K, respectively (Figure 9c). Increased C_{HV} from M-O-RSL further favors ablation by increasing the canopy air temperature (Figure 9c), which enhances the canopy air-to-ground temperature gradient that drives the sensible heat flux downward to the ground.

Conversely, over the CS site, the M-O-RSL scheme simulates slower ablation (Figures 8c, 8d, and 9h). This occurs because the M-O-RSL scheme results in smaller $C_{H\text{-}UC}$ (Figure 9e) that causes less downward sensible heat flux by 13 W/m² (median) and hence less heat flux into snowpack by 13 W/m² (median) (Figure 9f). This decreases snow temperatures causing slower snowmelt (Figures 9g and 9h). We note that decreases in L_H (Figure 9f) have a much smaller effect on snow ablation (Figure 8d). M-O-RSL predicts higher C_{HV} which increases the canopy air temperature and thus the canopy air-to-ground temperature gradient. However, this only partially offsets the ablation slow-down imposed by decreases in $C_{H\text{-}UC}$.

4.2. AmeriFlux Surface Energy Budget and Snow Evaluation

To evaluate the factors controlling seasonal snowpack evolution, we examine the relationship between modeled and observed SWE and surface energy budgets over two AmeriFlux sites: GLEES in Wyoming and NR in Colorado (Figures 10–12). At each site, we evaluate the surface energy budget (Equation 25) during the water year that M-O and M-O-RSL SWE are the most different: 2014 for GLEES and 2017 for NR (Figures S6 and S7).

At GLEES, M-O and M-O-RSL simulations overestimate surface albedo during the 2014 accumulation period, resulting in underestimates of absorbed shortwave radiation relative to observations during snow accumulation (Figure 10a and Table 1). This translates to underestimates in upward latent heat (L_H) and downward sensible heat (Q_H) flux which both contribute to overestimates in simulated peak SWE (Figures 10a and 11a and Table 1). The L_H bias alone accounts for a 79 mm low bias in sublimation for M-O and 83 mm for M-O-RSL over the 85-day accumulation period. This exceeds the 41 mm overestimate in peak SWE from M-O (Figures 11a). This inconsistency may be attributable to compensatory errors in models and observations (Chen et al., 2014). For example, undercatch with weighing-type gauges at SNOTEL sites have been found to contribute toward precipitation being underestimated by 10%–20% during winter months (Serreze et al., 2001; Yang et al., 1998) which would directly counteract the effects of overestimated albedo. It is also reasonable to assume that inconsistencies between surface energy budget and snowpack comparisons are
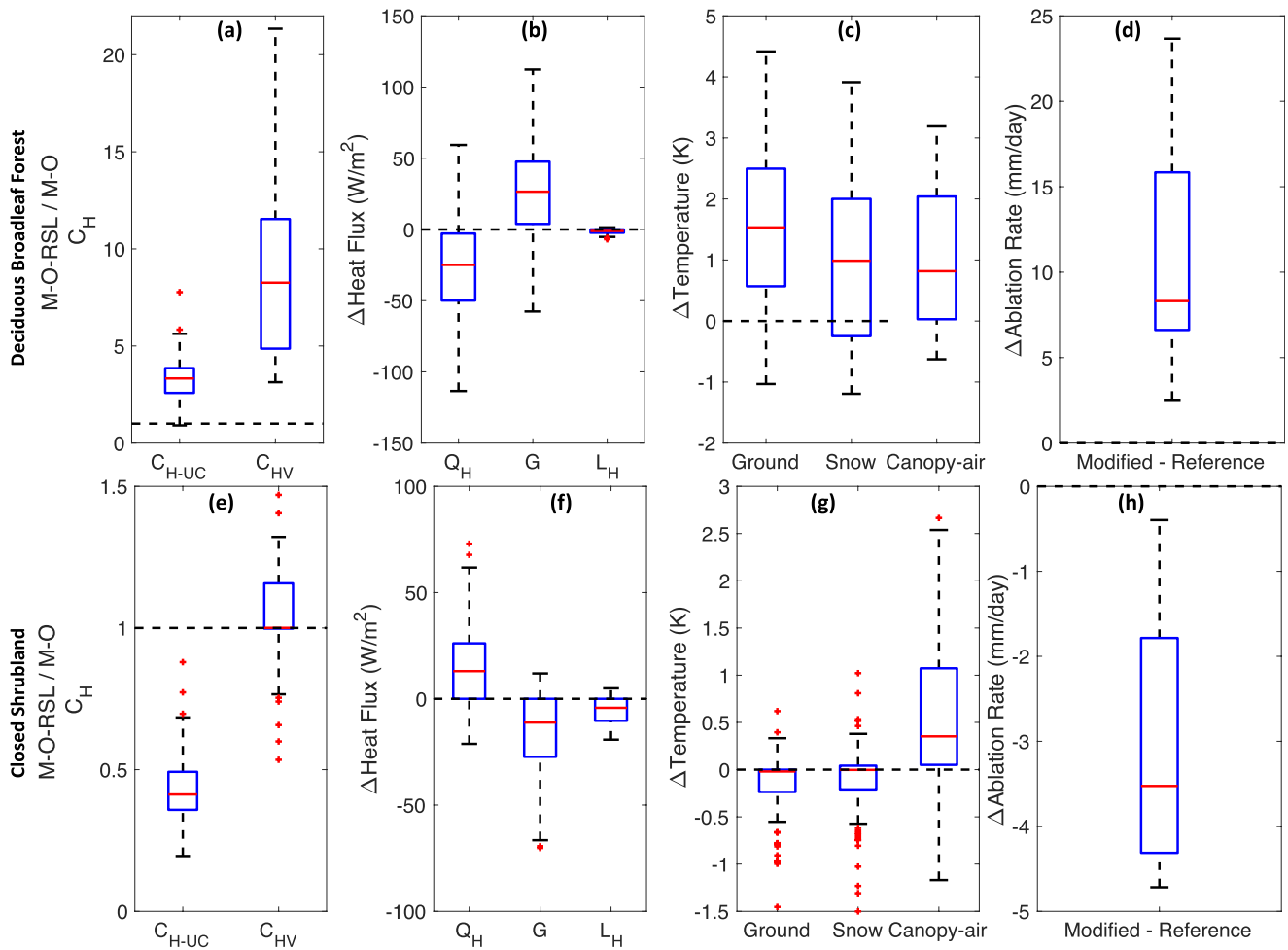
Figure 9. Differences in variables (Δ) are calculated as M-O-RSL minus M-O outputs from ablation periods. (a)–(d) are calculated from the representative deciduous broadleaf forest site and (e)–(h) are calculated over the representative closed shrubland site. (a, e) ratio of M-O-RSL to M-O surface heat exchange coefficient under the canopy top (C_{H-UC}; Equation 24) and above canopy (C_{HV}; Equation 14); (b, f) change in sensible heat flux (Q_H), heat flux into snow surface (G) and latent heat flux (L_H). (c, g) change in ground, snow and canopy air temperature. (d, h) change in ablation rates.

at least partially attributable to SWE observations being measured approximately 900 m from the Ameri-Flux site where vegetation density can differ. M-O-RSL predicts peak SWE to be 47 mm higher than M-O (Figures 11a) because M-O predicts faster snowmelt when temperatures are above freezing. For instance, M-O predicts 42 mm more snowmelt between April 8 and the day of peak SWE (May 15) than M-O-RSL because higher C_{H-UC} from M-O (Figures 11c) yields larger within- and below-canopy downwards Q_H (Figure S8) that drives greater heat flux into the snow (Figures 11d) that melts the snowpack more efficiently. During this period (April 8 to May 15), M-O-RSL understory sensible heat flux has smaller errors than M-O relative to observations (Figure S8); however, greater melt from M-O during this time compensates for underestimated sublimation throughout accumulation, which overall results in smaller errors between M-O simulated and observed peak SWE.

At GLEES, albedo biases persist into the 2014 ablation period, causing underestimates in absorbed short-wave radiation. These biases are partially accounted for with biases in L_H and absorbed longwave radiation (Figure 10b and Table 1). It is reasonable to assume that remaining albedo biases are accounted for with underestimates in simulated heat flux into the snow surface. However, this is difficult to confirm because this is not an observed quantity. These energy budget biases translate to biases in ablation rates: 27 mm/day for observations, 14 mm/day for M-O, and 16 mm/day for M-O-RSL (Figure 11a). M-O-RSL calculates higher heat flux into the snow surface and L_H relative to the M-O simulation, causing the 2 mm/day faster ablation rate than M-O (Figures 10b and 11a).
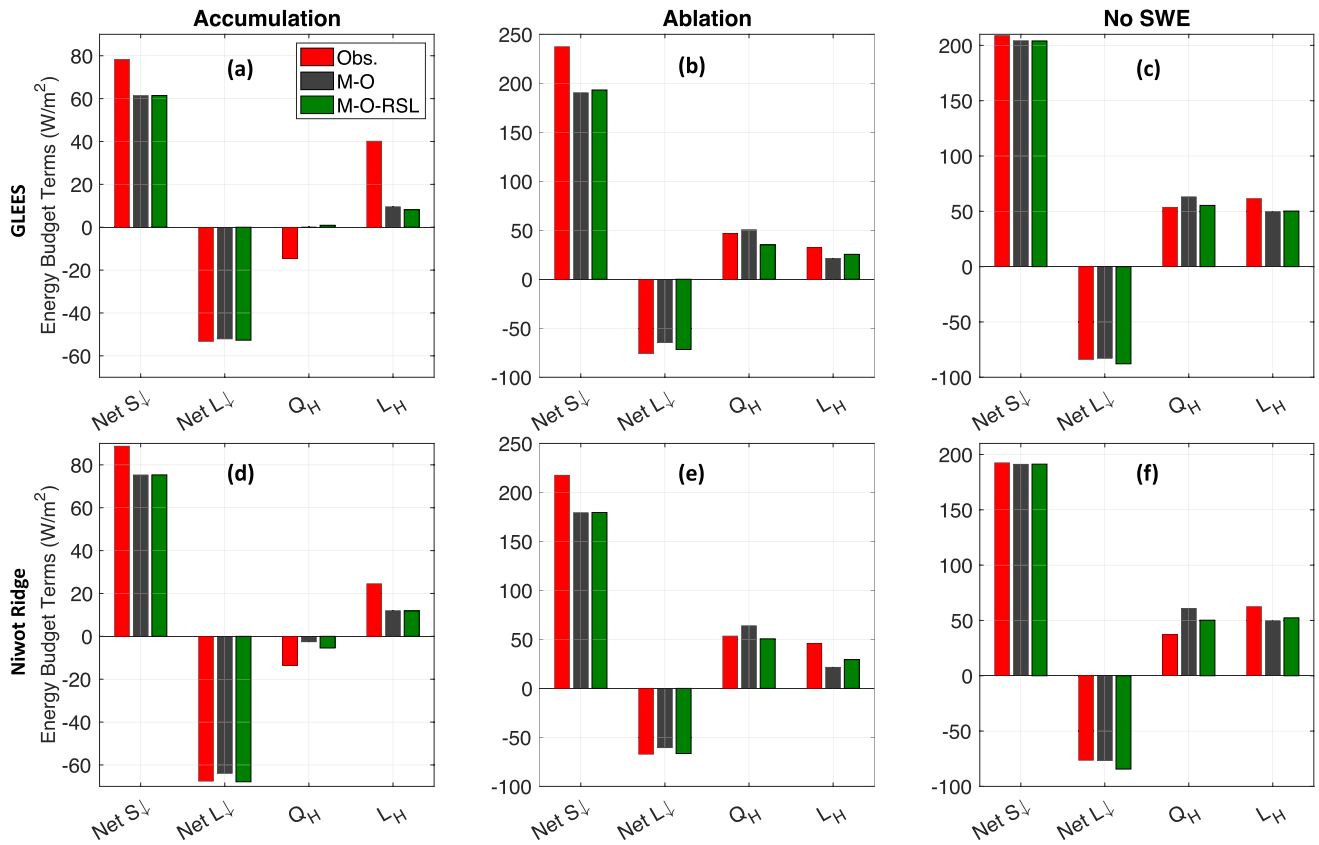
Figure 10. Absorbed solar radiation (Net $S\downarrow$), absorbed longwave radiation (Net $L\downarrow$), sensible heat flux (Q_H) and latent heat flux (L_H) for GLEES observations (red), M-O simulations (gray), and M-O-RSL simulations (green) during (a) accumulation and (b) ablation periods and (c) times with no snow over the 2014 water year. (d)–(f) same as (a)–(c) but for the 2017 water year from Niwot Ridge.

At NR, both M-O and M-O-RSL overestimate albedo relative to observations during the 2017 accumulation period, resulting in lower absorbed shortwave radiation and hence lower L_H and downwards Q_H that both contribute to overestimates of simulated peak SWE (Figures 10d and 12a and Table 1). The L_H bias alone accounts for a 27 and 28 mm underestimate of sublimation from M-O and M-O-RSL over the 72-day accumulation period, respectively. This accounts for 43% and 25% of peak SWE biases from M-O and M-O-RSL, respectively. It is reasonable to assume the majority of the remaining difference is accounted for by underestimated snowmelt driven by underestimated Q_H (Figure 10d and Table 1) and spatial heterogeneity in the snowpack between the AmeriFlux and the nearest neighbor SNOTEL station 350 m away (Burns et al., 2014). M-O-RSL predicts peak SWE to be 47 mm higher than M-O predictions during the 2017 WY (Figure 12a). At NR, M-O and M-O-RSL simulated SWE begin to diverge approximately 2-months before the day of peak SWE because temperatures are regularly above freezing beginning in early February (Figure 12b). Thus, beginning in February, discrepancies between M-O and M-O-RSL $C_{H\text{-}UC}$ (Figure 12c) translate to Q_H that drives the increased heat flux into the snowpack (Figure 12d) causing differences in snowmelt.

At NR, albedo errors persist into the 2017 ablation period, causing underestimates in absorbed shortwave radiation (Figure 10e and Table 1). These underestimates are partially balanced by underestimates in L_H (Figure 10e and Table 1). It is reasonable to assume that shortwave radiation biases that are not accounted for with biases in L_H are accounted for with underestimates in simulated heat flux into the snow surface. These energy budget biases drive slower simulated ablation rates, relative to observations: 7.9 mm/day for observations and 3.8 mm/day for M-O and M-O-RSL simulations (Figure 12a).

There is no dominant solution between M-O and M-O-RSL simulated energy budgets at GLEES and NR (Table 1). It is noteworthy that albedo errors are much smaller when snow is not present at both GLEES and
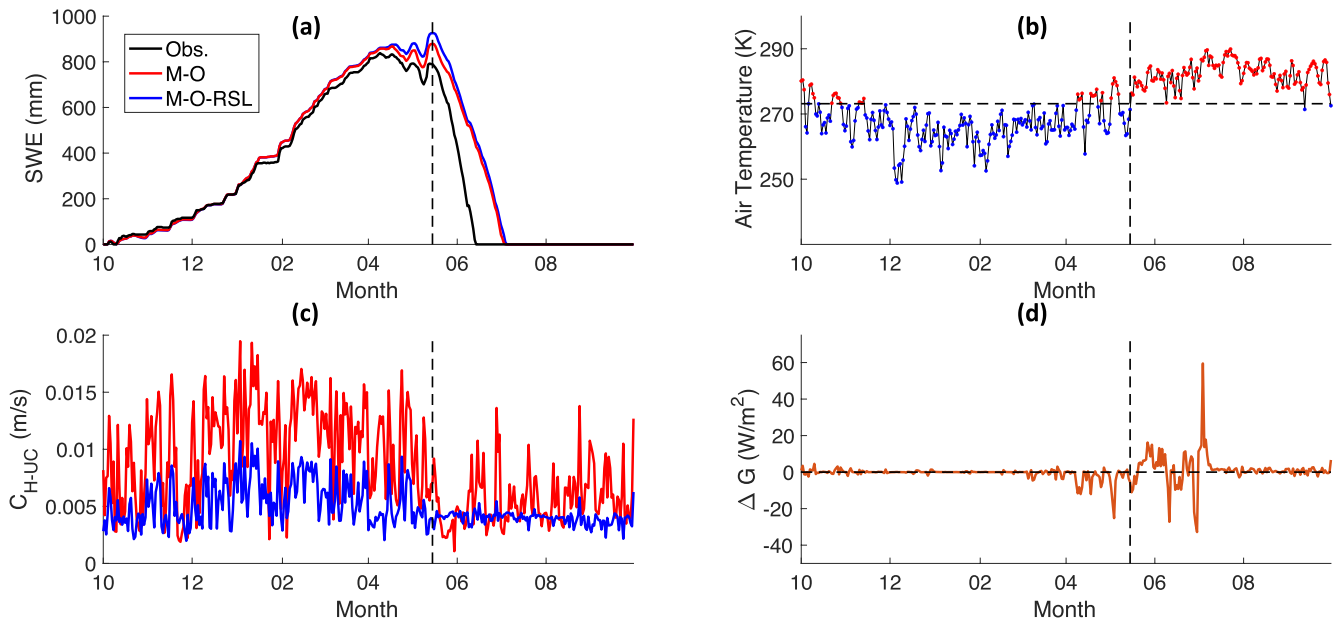
Figure 11. Variables in panels (a)–(d) cover the 2014 WY at GLEES and are used to interpret differences between M-O and M-O-RSL peak SWE. Vertical dashed black lines mark the day of peak SWE. (a) SWE from M-O (red) and M-O-RSL (blue) simulations. (b) Air temperature forcing M-O and M-O-RSL simulations. Red dots represent days when the mean daily temperature exceeds freezing, and blue dots represent days when the mean daily temperature is below freezing. The horizontal dashed line marks the freezing point (273.15K) (c) $C_{H\text{-}UC}$ from M-O (red) and M-O-RSL (blue) simulations. (d) M-O-RSL minus M-O G. Negative values indicate M-O is simulating more heat flux into the snowpack or soil (when there is no snow) than M-O-RSL.

NR (Figures 10c and 10f). This indicates that the discrepancies between simulated and observed albedo are attributable to errors in simulated snow cover and/or snow albedo computed using the CLASS physics option. The other Noah-MP snow surface albedo physics option (BATS) is known to produce even larger snow surface albedo than the CLASS option used herein, thus switching snow surface albedo physics options is
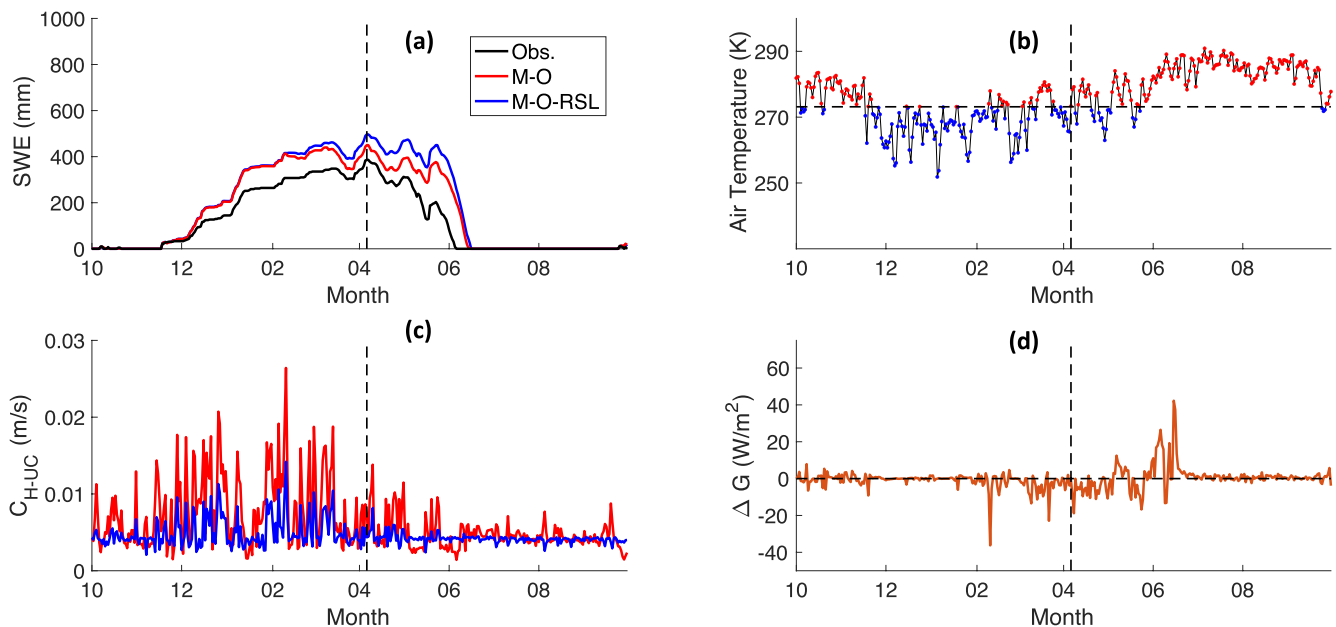

Figure 12. Variables in panels (a)–(d) cover the 2017 WY at NR and are used to interpret differences between M-O and M-O-RSL peak SWE. (a) SWE from M-O (red) and M-O-RSL (blue) simulations. (b) Air temperature forcing M-O and M-O-RSL simulations. Red dots represent days when the mean daily temperature exceeds freezing, and blue dots represent days when the mean daily temperature is below freezing. The horizontal dashed line marks the freezing point (273.15K) (c) $C_{H\text{-}UC}$ from M-O (red) and M-O-RSL (blue) simulations. (d) M-O-RSL minus M-O G. Negative values indicate M-O is simulating more heat flux into the snow and soil than M-O-RSL.

Table 1
Mean Bias and Correlation (R) Between Simulated and Observed Surface Energy Budget Terms Over Accumulation (Top) and Ablation Periods (Bottom)

	GLEES				Niwot ridge			
	Accumulation period							
	M-O		M-O-RSL		M-O		M-O-RSL	
	Bias (W/m²)	**R**	**Bias (W/m²)**	**R**	**Bias (W/m²)**	**R**	**Bias (W/m²)**	**R**
Net $S\downarrow$	−16.9	1.00	−16.9	1.00	−13.5	1.00	−13.5	1.00
Net $L\downarrow$	1.10	1.00	0.60	1.00	3.60	0.99	−0.30	1.00
Q_H	14.7	0.49	15.5	0.48	10.9	0.63	8.00	0.53
L_H	−30.7	0.41	−32.0	0.44	−12.6	0.72	−12.7	0.65
	Ablation period							
Net $S\downarrow$	−47.0	1.00	−44.2	1.00	−38.4	1.00	−38.1	1.00
Net $L\downarrow$	11.1	0.99	4.30	1.00	6.50	0.99	0.70	1.00
Q_H	3.50	0.63	−11.9	0.60	10.4	0.62	−2.90	0.48
L_H	−11.1	0.42	−7.10	−0.04	−24.4	0.45	−16.6	0.37

not expected to improve this issue (Niu et al., 2011). Although improving simulated snow cover and albedo is out of the scope of this study, it is an important topic we are evaluating in on-going research.

4.3. AmeriFlux Within-Canopy Wind Speed and Turbulent Heat Flux Analysis

At GLEES, M-O and M-O-RSL underestimate within-canopy wind speed by 68% and 60%, respectively, and M-O has a higher correlation with observed within-canopy wind speed than M-O-RSL (Figure 13a). Discrepancies between simulated and observed within-canopy wind speed are partially attributable to the actual canopy height at GLEES being lower than the Noah-MP default setting of H_{CAN} (20 m) for evergreen needle-leaf forests (Burns et al., 2021). M-O and M-O-RSL within-canopy wind speed predictions have smaller biases and higher correlations when H_{can} is set to a more accurate value (12 m) (Burns et al., 2021) (Figure 13b). Discrepancies that persist between simulated and observed within-canopy wind speed are likely affected by limitations imposed by the one-layer bulk canopy model structure of Noah-MP as well as violations of the HF08 dense canopy assumption (Bonan et al., 2021; Burns et al., 2018). Counterintuitively, despite M-O predicting lower within-canopy wind speed than M-O-RSL, M-O predicts larger below-canopy sensible heat
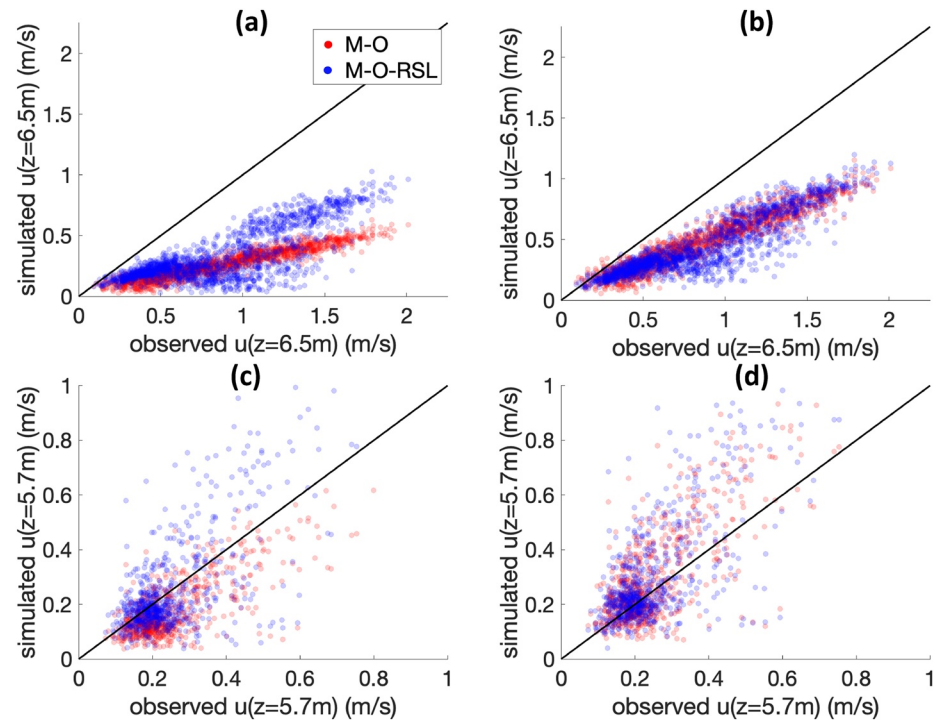

Figure 13. Scatter plots of observed within-canopy wind speed (horizontal axis) and simulated within-canopy wind speed (vertical axis) from M-O (red) and M-O-RSL (blue). The solid black line is a reference 1:1 line. For each panel, correlation coefficients (*R*) and percent bias from M-O and M-O-RSL simulations are recorded. (a) GLEES 6.5 m wind speed, when Noah-MP H_{CAN} is set to 20 m. *R*(M-O) = 0.94; *R*(M-O-RSL) = 0.77; Bias(M-O) = −68%; Bias(M-O-RSL) = −60%. (b) GLEES 6.5 m wind speed, when Noah-MP H_{CAN} is set to 12 m. *R*(M-O) = 0.95; *R*(M-O-RSL) = 0.89; Bias(M-O) = −42%; Bias(M-O-RSL) = −46% (c) Niwot Ridge 5.7 m wind speed, when Noah-MP H_{CAN} is set to 20 m. *R*(M-O) = 0.72; *R*(M-O-RSL) = 0.67; Bias(M-O) = −27%; Bias(M-O-RSL) = 0.8% (d) Niwot Ridge 5.7 m wind speed, when Noah-MP H_{CAN} is set to 12 m. *R*(M-O) = 0.73; *R*(M-O-RSL) = 0.70; Bias(M-O) = 18%; Bias(M-O-RSL) = 23%.

flux (Figure S8). This is attributable to M-O-RSL explicitly accounting for $ra_{hg\text{-}0}$ (Equation 20) which favors larger resistance to sensible heat flux from M-O-RSL compared to M-O; noting that $ra_{hg\text{-}0}$ accounts for 49% of total ra_{hg} at GLEES in the M-O-RSL simulation.

At NR, M-O underestimates wind speed by 27% and M-O-RSL overestimates wind speed by 0.8% (Figure 13c). The underestimation of wind speed at M-O is partially attributable to the actual canopy height at NR being lower than the H_{CAN} for evergreen needleleaf forests used in Noah-MP (Burns et al., 2018). M-O and M-O-RSL overestimate wind speed (by 18% and 23%, respectively) when H_{CAN} is set to a more accurate height (12m) (Burns et al., 2018) (Figure 13d). However, both M-O and M-O-RSL have increased correlations corresponding with the H_{CAN} adjustment. M-O and M-O-RSL have lower correlations with observed wind speed at NR than at GLEES which is likely attributable to the assumed linearity between above-canopy friction velocity and within-canopy wind speed being violated at NR (Burns et al., 2018); whereas this assumption is reasonable at GLEES (Figure S10). Similar to GLEES, M-O-RSL predicts higher within-canopy wind speed at NR and lower within-canopy sensible heat flux than M-O due to M-O-RSL explicitly accounting for $ra_{hg\text{-}0}$; noting that $ra_{hg\text{-}0}$ accounts for 51% of total ra_{hg} at NR in the M-O-RSL simulation (Figures 13 and S9).

5. Conclusions and Implications

This study implemented a new surface exchange physics scheme into the Noah-MP LSM that accounts for canopy-induced turbulence in the RSL based on a modified version of the MOST following methodologies of Harman and Finnigan (2007, 2008) and Bonan et al. (2018). Noah-MP simulations that used the default M-O scheme (i.e., M-O simulations) were compared with simulations that used the new M-O-RSL scheme (i.e., M-O-RSL simulations) over 647 SNOTEL stations and 2 AmeriFlux stations. The primary interest of this study was to evaluate M-O-RSL snowpack simulations, benchmarked against M-O simulations. Overall, M-O-RSL simulations tend to have better agreement with observed snowpack and energy fluxes than M-O simulations, although there is heterogeneity in results across different sites. Specifically, SWE simulated from M-O-RSL has higher correlation and lower RMSE with SNOTEL observed SWE at 69% and 65% of the study sites, respectively, compared to M-O. M-O-RSL performance is likely limited by the Noah-MP one-layer bulk canopy assumption because the HF08 methodology (Harman & Finnigan, 2007, 2008) is most appropriately applied in a multilayer model that considers heterogeneity in the vegetated vertical profile (Bonan et al., 2021).

Differences between M-O and M-O-RSL simulated snowpack are primarily attributable to differences in $C_{H\text{-}UC}$, which controls downward sensible heat flux to the ground and hence heat flux into snowpack. Differences in heat flux into snowpack drive differences in snowmelt when temperatures are close to or above the melting point, which typically occurs late in accumulation periods and throughout ablation periods. Differences in $C_{H\text{-}UC}$ are a product of M-O-RSL accounting for canopy-induced turbulence as well as explicit consideration of aerodynamic resistance for heat directly above the land surface. The largest improvements for M-O-RSL occur over closed shrubland sites, and the largest degradations for M-O-RSL occur over deciduous broadleaf forest sites. Over closed shrubland sites, M-O-RSL tends to simulate smaller $C_{H\text{-}UC}$, and thus less snowmelt than M-O. Conversely, over deciduous broadleaf forest sites, M-O-RSL tends to simulate larger $C_{H\text{-}UC}$, and thus more snowmelt than M-O. Degraded performance over DBF sites is reflective of the fact that the M-O-RSL scheme is developed by assuming a dense canopy; an assumption that is violated over DBF sites in winter.

Based on the surface energy budget analysis over GLEES and NR stations, differences between M-O and M-O-RSL can be overwhelmed by biases that do not relate to the new canopy turbulence scheme. For example, when snow is present, both M-O and M-O-RSL simulations overestimate surface albedo which dominates errors in the simulated surface energy budget and snowpack. Toward the goal of improving the representation of surface albedo in Noah-MP, we are conducting on-going research focused on improving the albedo formulation in Noah-MP guided by observed incoming and outgoing shortwave radiation at both visible and near infra-red wavelength bands at a high-elevation site in Colorado.

M-O tends to more accurately predict wind speed within the canopy than M-O-RSL. This is likely because the HF08 methodology, which the M-O-RSL is based on, was designed with a greater emphasis on improving above-canopy fluxes rather than within- and below-canopy fluxes, and thus HF08 is less accurate

underneath the canopy top where vegetation density is more complex (Harman & Finnigan, 2007, 2008). Differences in understory wind speed from M-O and M-O-RSL do not dictate differences in understory sensible heat flux, primarily because M-O-RSL explicitly accounts for aerodynamic resistance to sensible heat flux directly over the land surface and M-O does not. Hence, higher understory wind speed in M-O-RSL does not necessarily favor greater understory sensible heat flux.

We intend for the M-O-RSL physics scheme to improve weather and hydrological applications for models such as WRF and the National Water Model, and improve estimates of model uncertainty. We expect M-O-RSL to be considered in the future multi-model ensemble studies, similar to Zhang et al. (2016) and You et al. (2020), that employed Noah-MP to quantify uncertainty based on different combinations of physics options. Furthermore, the Noah-MP modeling community will benefit from a new surface exchange scheme that accounts for canopy-induced turbulence in the RSL which has been shown to improve model agreement with the majority of SNOTEL snowpack observations. Future work that optimizes tunable parameters for Noah-MP simulations using the M-O-RSL physics option should consider the sensitivities to z_1 and H_{CAN} that are discussed in this manuscript.

Conflict of Interest

The authors declare no conflicts of interest relevant to this study.

Data Availability Statement

The authors thank Gordon Bonan for sharing data, code, and insights. The authors thank Edward (Ned) Patton for sharing insights on the roughness sublayer turbulence theory and model implementation. The authors thank Peter Blanken for sharing insights on data uncertainty and within-canopy observations from the US-NR1 AmeriFlux site. Simulation data used in this manuscript are available on Mendeley Data (Abolafia-Rosenzweig et al., 2021). The study and its presentation benefitted from the review comments of two anonymous reviewers communicated through correspondence with editor Dr. Eleanor Blyth.

References

Abolafia-Rosenzweig, R., He, C., & Chen, F. (2021). *Implementation and evaluation of a unified turbulence parameterization throughout the canopy and roughness sublayer in Noah-MP snow simulations* (p. V2). Mendeley Data. https://doi.org/10.17632/y7j2h66wz7.1

Barlage, M., Chen, F., Tewari, M., Ikeda, K., Gochis, D., Dudhia, J., et al. (2010). Noah land surface model modifications to improve snowpack prediction in the Colorado Rocky Mountains. *Journal of Geophysical Research*, *115*, D22101. https://doi.org/10.1029/2009JD013470

Blanken, P., Monson, R. K., Burns, S. P., Bowling, D. R., & Turnipseed, A. A. (2020). *AmeriFlux US-NR1 Niwot Ridge Forest (LTER NWT1)* (Ver. 16-5). AmeriFlux AMP. (Dataset). https://doi.org/10.17190/AMF/1246088

Bonan, G. B. (1996). *A Land Surface Model (LSM Version 1.0) for ecological, hydrological and atmospheric studies: Technical description and user's guide. NCAR Technical Note T. N.-417+STR*. National Center for Atmospheric Research.

Bonan, G. B., Patton, E. G., Finnigan, J. J., Baldocchi, D. D., & Harman, I. N. (2021). Moving beyond the incorrect but useful paradigm: Reevaluating big-leaf and multilayer plant canopies to model biosphere-atmosphere fluxes – A review. *Agricultural and Forest Meteorology*, *306*, 108435. https://doi.org/10.1016/j.agrformet.2021.108435

Bonan, G. B., Patton, E. G., Harman, I. N., Oleson, K. W., Finnigan, J. J., Lu, Y., & Burakowski, E. A. (2018). Modeling canopy-induced turbulence in the Earth system: A unified parameterization of turbulent exchange within plant canopies and the roughness sublayer (CLM-ml v0). *Geoscientific Model Development*, *11*, 1467–1496. https://doi.org/10.5194/gmd-11-1467-2018

Brutsaert, W. (1982). *Evaporation into the atmosphere*. Springer Netherlands. https://doi.org/10.1007/978-94-017-1497-6

Burns, S. P., Frank, J. M., Massman, W., Patton, E. G., & Blanken, P. (2021). The effect of static pressure-wind covariance on vertical carbon dioxide exchange at a windy subalpine forest site. *Agricultural and Forest Meteorology*, *306*, 108402. https://doi.org/10.1016/j.agrformet.2021.108402

Burns, S. P., Molotch, N. P., Williams, M. W., Knowles, J. F., Seok, B., Monson, R. K., et al. (2014). Snow temperature changes within a seasonal snowpack and their relationship to turbulent fluxes of sensible and latent heat. *Journal of Hydrometeorology*, *15*, 117–142. https://doi.org/10.1175/JHM-D-13-026.1

Burns, S. P., Swenson, S. C., Wieder, W. R., Lawrence, D. M., Bonan, G. B., Knowles, J. F., & Blanken, P. D. (2018). A comparison of the diel cycle of modeled and measured latent heat flux during the warm season in a Colorado Subalpine Forest. *Journal of Advances in Modeling Earth Systems*, *10*, 617–651. https://doi.org/10.1002/2017MS001248

Chen, F., Barlage, M., Tewari, M., Rasmussen, R., Jin, J., Lettenmaier, D., et al. (2014). Modeling seasonal snowpack evolution in the complex terrain and forested Colorado Headwaters region: A model intercomparison study. *Journal of Geophysical Research: Atmospheres*, *119*(24), 13795–13819. https://doi.org/10.1002/2014JD022167

Chen, F., & Dudhia, J. (2001). Coupling an advanced land surface–hydrology model with the Penn State–NCAR MM5 Modeling System. Part I: Model implementation and sensitivity. *Monthly Weather Review*, *129*, 17. https://doi.org/10.1175/1520-0493(2001)129<0569:caalsh>2.0.co;2

Chen, F., Janjić, Z., & Mitchell, K. (1997). Impact of atmospheric surface-layer parameterizations in the new land-surface scheme of the NCEP Mesoscale Eta Model. *Boundary-Layer Meteorology*, *85*, 391–421. https://doi.org/10.1023/A:1000531001463

Chen, F., Mitchell, K., Schaake, J., Xue, Y., Pan, H.-L., Koren, V., et al. (1996). Modeling of land surface evaporation by four schemes and comparison with FIFE observations. *Journal of Geophysical Research: Atmospheres*, *101*, 7251–7268. https://doi.org/10.1029/95JD02165

Chotamonsak, C., Salathé, E. P., Kreasuwan, J., Chantara, S., & Siriwitayakorn, K. (2011). Projected climate change over Southeast Asia simulated using a WRF regional climate model. *Atmospheric Science Letters*, *12*, 213–219. https://doi.org/10.1002/asl.313

Cohen, J. (1994). Snow cover and climate. *Weather*, *49*, 150–156. https://doi.org/10.1002/j.1477-8696.1994.tb05997.x

Dong, C. (2018). Remote sensing, hydrological modeling and in situ observations in snow cover research: A review. *Journal of Hydrology*, *561*, 573–583. https://doi.org/10.1016/j.jhydrol.2018.04.027

Ek, M. B., Mitchell, K. E., Lin, Y., Rogers, E., Grunmann, P., Koren, V., et al. (2003). Implementation of Noah land surface model advances in the National Centers for Environmental Prediction operational mesoscale Eta model. *Journal of Geophysical Research: Atmospheres*, *108*, 2002JD003296. https://doi.org/10.1029/2002JD003296

Fazu, C., & Schwerdtfeger, P. (1989). Flux-gradient relationships for momentum and heat over a rough natural surface. *Quarterly Journal of the Royal Meteorological Society*, *115*, 335–352. https://doi.org/10.1002/qj.49711548607

Finnigan, J. J., & Shaw, R. H. (2000). A wind-tunnel study of airflow in waving wheat: An EOF analysis of the structure of the Large-Eddy Motion. *Boundary-Layer Meteorology*, *96*, 211–255. https://doi.org/10.1023/A:1002618621171

Finnigan, J. J., Shaw, R. H., & Patton, E. G. (2009). Turbulence structure above a vegetation canopy. *Journal of Fluid Mechanics*, *637*, 387–424. https://doi.org/10.1017/S0022112009990589

Frank, J. M., Massman, W. J., Ewers, B. E., Huckaby, L. S., & Negron, J. F. (2014). Ecosystem CO_2/H_2O fluxes are explained by hydraulically limited gas exchange during tree mortality from spruce bark beetles. *Journal of Geophysical Research*, *119*, 1195–1215. https://doi.org/10.1002/2013JG002597

Franz, K. J., Hogue, T. S., & Sorooshian, S. (2008). Operational snow modeling: Addressing the challenges of an energy balance model for National Weather Service forecasts. *Journal of Hydrology*, *360*, 48–66. https://doi.org/10.1016/j.jhydrol.2008.07.013

Garratt, J. (1994). Review: The atmospheric boundary layer. *Earth-Science Reviews*, *37*, 89–134. https://doi.org/10.1016/0012-8252(94)90026-4

Garratt, J. R. (1978). Flux profile relations above tall vegetation. *Quarterly Journal of the Royal Meteorological Society*, *104*, 199–211. https://doi.org/10.1002/qj.49710443915

Gochis, D., Yu, W., & Yates, D. (2015). *The WRF-Hydro model technical description and user's guide, version 3.0* (p. 120). NCAR Tech. Doc. http://www.ral.ucar.edu/projects/wrf_hydro/

Goudriaan, J. (1977). *Crop micrometeoroloqy: A simulation study*. Wageningen: Wageningen Center for Agricultural Publishing and Documentation.

Harman, I. N. (2012). The role of roughness sublayer dynamics within surface exchange schemes. *Boundary-Layer Meteorology*, *142*, 1–20. https://doi.org/10.1007/s10546-011-9651-z

Harman, I. N., & Finnigan, J. J. (2007). A simple unified theory for flow in the canopy and roughness sublayer. *Boundary-Layer Meteorology*, *123*, 339–363. https://doi.org/10.1007/s10546-006-9145-6

Harman, I. N., & Finnigan, J. J. (2008). Scalar concentration profiles in the canopy and roughness sublayer. *Boundary-Layer Meteorology*, *129*, 323–351. https://doi.org/10.1007/s10546-008-9328-4

He, C., Chen, F., Barlage, M., Liu, C., Newman, A., Tang, W., et al. (2019). Can convection-permitting modeling provide decent precipitation for offline high-resolution snowpack simulations over mountains? *Journal of Geophysical Research: Atmospheres*, *124*, 12631–12654. https://doi.org/10.1029/2019JD030823

Högström, U. (1996). Review of some basic characteristics of the atmospheric surface layer. *Boundary-Layer Meteorology*, *78*, 215–246. https://doi.org/10.1007/bf00120937

Hong, S., Yu, X., Park, S. K., Choi, Y.-S., & Myoung, B. (2014). Assessing optimal set of implemented physical parameterization schemes in a multi-physics land surface model using genetic algorithm. *Geoscientific Model Development*, *7*, 2517–2529. https://doi.org/10.5194/gmd-7-2517-2014

Huning, L. S., & AghaKouchak, A. (2020). Global snow drought hot spots and characteristics. *Proceedings of the National Academy of Sciences of the United States of America*, *117*, 19753–19759. https://doi.org/10.1073/pnas.1915921117

Ikeda, K., Rasmussen, R., Liu, C., Newman, A., Chen, F., Barlage, M., et al. (2021). Snowfall and snowpack in the Western U.S. as captured by convection resolving current climate and pseudo global warming future climate simulations. *Climate Dynamics*, *57*, 1–25.

Jiang, Y., Chen, F., Gao, Y., He, C., Barlage, M., & Huang, W. (2020). Assessment of uncertainty sources in snow cover simulation in the Tibetan Plateau. *Journal of Geophysical Research: Atmospheres*, *125*. https://doi.org/10.1029/2020JD032674

Jordan, R. (1991). *A One-Dimensional Temperature Model for a Snow Cover: Technical Documentation for SNTHERM.89* (91-16, p. 49). U.S. Army Cold Regions Research and Engineering Laboratory Special Rep.

Kurkute, S., Li, Z., Li, Y., & Huo, F. (2020). Assessment and projection of water budget over Western Canada using convection permitting WRF simulations. *Hydrometeorology/Modelling approaches*, *24*, 3677–3697. https://doi.org/10.5194/hess-2019-522

Li, J., Chen, F., Lu, X., Gong, W., Zhang, G., & Gan, Y. (2020). Quantifying contributions of uncertainties in physical parameterization schemes and model parameters to overall errors in Noah-MP dynamic vegetation modeling. *Journal of Advances in Modeling Earth Systems*, *12*. https://doi.org/10.1029/2019MS001914

Li, J., Zhang, G., Chen, F., Peng, X., & Gan, Y. (2019). Evaluation of land surface subprocesses and their impacts on model performance with global flux data. *Journal of Advances in Modeling Earth Systems*, *11*, 1329–1348. https://doi.org/10.1029/2018MS001606

Liston, G. E., & Elder, K. (2006). A meteorological distribution system for high-resolution terrestrial modeling (MicroMet). *Journal of Hydrometeorology*, *7*, 217–234. https://doi.org/10.1175/JHM486.1

Liu, C., Ikeda, K., Rasmussen, R., Barlage, M., Newman, A. J., Prein, A. F., et al. (2017). Continental-scale convection-permitting modeling of the current and future climate of North America. *Climate Dynamics*, *49*, 71–95. https://doi.org/10.1007/s00382-016-3327-9

Livneh, B., Rosenberg, E. A., Lin, C., Nijssen, B., Mishra, V., Andreadis, K. M., et al. (2013). A long-term hydrologically based dataset of land surface fluxes and states for the conterminous United States: Update and extensions. *Journal of Climate*, *26*, 9384–9392. https://doi.org/10.1175/JCLI-D-12-00508.1

Livneh, B., Xia, Y., Mitchell, K. E., Ek, M. B., & Lettenmaier, D. P. (2010). Noah LSM snow model diagnostics and enhancements. *Journal of Hydrometeorology*, *11*, 721–738. https://doi.org/10.1175/2009JHM1174.1

Mahat, V., Tarboton, D. G., & Molotch, N. P. (2013). Testing above- and below-canopy representations of turbulent fluxes in an energy balance snowmelt model. *Water Resources Research*, *49*, 1107–1122. https://doi.org/10.1002/wrcr.20073

Massman, W. J. (2021). *AmeriFlux US-GLE GLEES* (Ver 8-5). AmeriFlux AMP. (Dataset). https://doi.org/10.17190/AMF/1246056

Maurer, E. P., Wood, A. W., Adam, J. C., Lettenmaier, D. P., & Nijssen, B. (2002). A long-term hydrologically based dataset of land surface fluxes and states for the conterminous United States. *Journal of Climate*, *15*, 15. https://doi.org/10.1175/1520-0442(2002)015<3237:althbd>2.0.co;2

Monin, A. S., & Obukhov, A. M. (1954). Basic laws of turbulent mixing in the surface layer of the atmosphere 30.

Mote, P. W. (2003). Trends in snow water equivalent in the Pacific Northwest and their climatic causes. *Geophysical Research Letters*, *30*. https://doi.org/10.1029/2003GL017258

Niu, G.-Y., & Yang, Z.-L. (2004). Effects of vegetation canopy processes on snow surface energy and mass balances. *Journal of Geophysical Research: Atmospheres*, *109*. https://doi.org/10.1029/2004JD004884

Niu, G.-Y., Yang, Z.-L., Mitchell, K. E., Chen, F., Ek, M. B., Barlage, M., et al. (2011). The community Noah land surface model with multiparameterization options (Noah-MP): 1. Model description and evaluation with local-scale measurements. *Journal of Geophysical Research*, *116*, D12109. https://doi.org/10.1029/2010JD015139

Novick, K. A., & Katul, G. G. (2020). The duality of reforestation impacts on surface and air temperature. *Journal of Geophysical Research: Biogeosciences*, *125*. https://doi.org/10.1029/2019JG005543

Pan, M., Sheffield, J., Wood, E. F., Mitchell, K. E., Houser, P. R., Schaake, J.C., et al. (2003). Snow process modeling in the North American Land Data Assimilation System (NLDAS): 2. Evaluation of model simulated snow water equivalent. *Journal of Geophysical Research: Atmospheres*, *108*, 2003JD003994. https://doi.org/10.1029/2003JD003994

Peters-Lidard, C. D., Mocko, D. M., Su, L., Lettenmaier, D. P., Gentine, P., & Barlage, M. (2021). Advances in land surface models and indicators for drought monitoring and prediction. *Bulletin of the American Meteorological Society*, 1–68. https://doi.org/10.1175/BAMS-D-20-0087.1

Rasmussen, R., Liu, C., Ikeda, K., Gochis, D., Yates, D., Chen, F., et al. (2011). High-resolution coupled climate runoff simulations of seasonal snowfall over Colorado: A process study of current and warmer climate. *Journal of Climate*, *24*, 3015–3048. https://doi.org/10.1175/2010JCLI3985.1

Raupach, M. R., Finnigan, J. J., & Brunet, Y. (1996). Coherent eddies and turbulence in vegetation canopies: The mixing layer analogy. *Boundary-Layer Meteorology*, *78*, 351–382. https://doi.org/10.1007/bf00120941

Raupach, M. R., & Thom, A. S. (1981). Turbulence in and above Plant Canopies. *Annual Review of Fluid Mechanics*, *13*, 97–129. https://doi.org/10.1146/annurev.fl.13.010181.000525

Robinson, A. R., & Lermusiaux, P. F. J. (2000). Overview of data assimilation. *Harvard Reports in Physical/Interdisciplinary (Ocean Sciences); The Division of Engineering and Applied Sciences*. Harvard University.

Sen Gupta, A., & Tarboton, D. G. (2016). A tool for downscaling weather data from large-grid reanalysis products to finer spatial scales for distributed hydrological applications. *Environmental Modelling & Software*, *84*, 50–69. https://doi.org/10.1016/j.envsoft.2016.06.014

Serreze, M. C., Clark, M. P., Armstrong, R. L., McGinnis, D. A., & Pulwarty, R. S. (1999). Characteristics of the western United States snowpack from snowpack telemetry (SNOTEL) data. *Water Resources Research*, *35*, 2145–2160. https://doi.org/10.1029/1999WR900090

Serreze, M. C., Clark, M. P., & Frei, A. (2001). Characteristics of large snowfall events in the montane western United States as examined using snowpack telemetry (SNOTEL) data. *Water Resources Research*, *37*, 675–688. https://doi.org/10.1029/2000WR900307

Shapkalijevski, M., Moene, A. F., Ouwersloot, H. G., Patton, E. G., & Vilà-Guerau de Arellano, J. (2016). Influence of canopy seasonal changes on turbulence parameterization within the roughness sublayer over an orchard canopy. *Journal of Applied Meteorology and Climatology*, *55*, 1391–1407. https://doi.org/10.1175/JAMC-D-15-0205.1

Sheffield, J., Xia, Y., Luo, L., Wood, E. F., Ek, M., & Mitchell, K. E. (2012). North American land data assimilation System: A framework for merging model and satellite data for improved drought monitoring, 43.

Sun, N., Yan, H., Wigmosta, M., Skaggs, R., Leung, R., & Hou, Z. (2019). Regional snow parameters estimation for large-domain hydrological applications in the western United States. *Journal of Geophysical Research: Atmospheres*, *124*, 5296–5313. https://doi.org/10.1029/2018JD030140

Thom, A. S., Stewart, J. B., Oliver, H. R., & Gash, J. H. C. (1975). Comparison of aerodynamic and energy budget estimates of fluxes over a pine forest. *Quarterly Journal of the Royal Meteorological Society*, *101*, 93–105. https://doi.org/10.1002/qj.49710142708

Viterbo, F., Mahoney, K., Read, L., Salas, F., Bates, B., Elliott, J., et al. (2020). A multiscale, hydrometeorological forecast evaluation of National Water Model Forecasts of the May 2018 Ellicott City, Maryland, Flood. *Journal of Hydrometeorology*, *21*, 475–499. https://doi.org/10.1175/JHM-D-19-0125.1

Wickham, J., Stehman, S. V., Sorenson, D. G., Gass, L., & Dewitz, J. A. (2021). Thematic accuracy assessment of the NLCD 2016 land cover for the conterminous United States. *Remote Sensing of Environment*, *257*, 112357. https://doi.org/10.1016/j.rse.2021.112357

Xia, Y., Ek, M., Wei, H., & Meng, J. (2012). Comparative analysis of relationships between NLDAS-2 forcings and model outputs. *Hydrological Processes*, *26*, 467–474. https://doi.org/10.1002/hyp.8240

Xia, Y., Mitchell, K., Ek, M., Sheffield, J., Cosgrove, B., Wood, E., et al. (2009). *NLDAS primary forcing data L4 hourly 0.125 x 0.125 degree V002*. NASA/GSFC/HSL. Goddard Earth Sciences Data and Information Services Center (GES DISC). Accessed December 12, 2020. https://doi.org/10.5067/6J5LHHOHZHN4

Xia, Y., Mitchell, K., Ek, M., Cosgrove, B., Sheffield, J., Luo, L., et al. (2012). Continental-scale water and energy flux analysis and validation for North American Land Data Assimilation System project phase 2 (NLDAS-2): 2. Validation of model-simulated streamflow. *Journal of Geophysical Research: Atmospheres*, *117*. https://doi.org/10.1029/2011JD016051

Xia, Y., Peter-Lidard, C. D., Huang, M., Wei, H., & Ek, M. (2015). Improved NLDAS-2 Noah-simulated hydrometeorological products with an interim run. *Hydrological Processes*, *29*, 780–792. https://doi.org/10.1002/hyp.10190

Xiao, M., Mahanama, S. P., Xue, Y., Chen, F., & Lettenmaier, D. P. (2021). Modeling snow ablation over the mountains of the Western United States: Patterns and controlling factors. *Journal of Hydrometeorology*, *22*, 297–311. https://doi.org/10.1175/JHM-D-19-0198.1

Yan, H., Sun, N., Wigmosta, M., Skaggs, R., Hou, Z., & Leung, R. (2018). Next-generation intensity-duration-frequency curves for hydrologic design in snow-dominated environments. *Water Resources Research*, *54*(2), 1093–1108. https://doi.org/10.1002/2017wr021290

Yang, D., Goodison, B. E., Metcalfe, J. R., Golubev, V.S., Bates, R., Pangburn, T., Hanson, C. L., (1998). Accuracy of NWS 8" Standard Nonrecording Precipitation Gauge: Results and Application of WMO Intercomparison. *Journal of Atmospheric Ocean Technology*, *15*, 15.

Yang, Z.-L., Niu, G.-Y., Mitchell, K. E., Chen, F., Ek, M. B., Barlage, M., et al. (2011). The community Noah land surface model with multiparameterization options (Noah-MP): 2. Evaluation over global river basins. *Journal of Geophysical Research*, *116*, D12110. https://doi.org/10.1029/2010JD015140

Yi, C. (2008). Momentum transfer within canopies. *Journal of Applied Meteorology and Climatology*, *47*, 262–275. https://doi.org/10.1175/2007JAMC1667.1

You, Y., Huang, C., Gu, J., Li, H., Hao, X., & Hou, J. (2020). Assessing snow simulation performance of typical combination schemes within Noah-MP in northern Xinjiang, China. *Journal of Hydrology*, *581*, 124380. https://doi.org/10.1016/j.jhydrol.2019.124380

Zhang, G., Chen, F., Chen, Y., Li, J., & Peng, X. (2020). Evaluation of Noah-MP land-model uncertainties over sparsely vegetated sites on the Tibet Plateau. *Atmosphere*, *11*, 458. https://doi.org/10.3390/atmos11050458

Zhang, G., Chen, F., & Gan, Y. (2016). Assessing uncertainties in the Noah-MP ensemble simulations of a cropland site during the Tibet Joint International Cooperation program field campaign. *Journal of Geophysical Research: Atmospheres*, *121*, 9576–9596. https://doi.org/10.1002/2016JD024928

Zhang, Y., Pan, M., Sheffield, J., Siemann, A. L., Fisher, C. K., Liang, M., et al. (2018). A Climate Data Record (CDR) for the global terrestrial water budget: 1984–2010. *Hydrology and Earth System Sciences*, *22*, 241–263. https://doi.org/10.5194/hess-22-241-2018